Development Of A Blood Shear Stress Device Using Numerical & Experimental Methods

by

Shweta Karnik

A thesis submitted to the Department of Mechanical Engineering,

University of Houston

in partial fulfillment of the requirements for the degree of

Master of Science

in Mechanical Engineering

Chair of Committee: Dr. Ralph W. Metcalfe

Committee Member: Dr. Shailendra Joshi

Committee Member: Dr. Annalisa Quaini

University of Houston

May 2020

ACKNOWLEDGEMENTS

I would firstly like to express my gratitude towards my thesis advisor, Dr. Ralph Metcalfe for his continuous support and guidance during my graduate degree. I am thankful to him for introducing me to the research opportunity at Texas Heart Institute, and I really appreciate his patience while working along with me on this research.

I would also like to thank Dr. P. Alex Smith and Dr. Yaxin Wang for giving me an opportunity to work on this research grant at Texas Heart Institute, and for sharing their knowledge related to experimental and FEM study. I am grateful to Dr. Nobu Kurita for teaching me the basics of magnetism, and to Dr. Katharine Fraser for solving my doubts related to the computational fluid dynamics involved in this project.

I would also like to extend my sincere gratitude to my thesis committee members, Dr. Shailendra Joshi and Dr. Annalisa Quaini for taking their valuable time out and giving me their insightful suggestions and encouragement.

Lastly, I would like to thank my family especially my pet, Grace for the unconditional love and support from across the nation.

ABSTRACT

Left Ventricular Assist Devices (LVADs) are mechanical pumps used to treat heart failure, which is the cause of 6.2 million deaths in the United States every year. Despite clinical success, the capability of LVADs to operate successfully without causing blood damage remains a challenge. Due to high fluid stresses for prolonged period, the circulatory components of a LVAD tend to cause mechanical destruction of red blood cells leading to the release of hemoglobin into the bloodstream, termed as hemolysis. We have developed a Blood Shear Stress Device (BSSD) for LVAD component testing which will aid in identifying the amount of blood damage caused and its source. This device will enable individual component analysis thereby improving LVAD design while simultaneously reducing development time and cost. The BSSD consists of an active and passive magnetic levitation system for the brushless DC (BLDC) motor and uses a large gap between the BLDC motor components as a blood flow region for the component testing of LVADs. The passive magnetic levitation system is comprised of two concentric permanent magnet bearings used to stabilize the BLDC motor radially. The development process of this device involved magnetic modelling using numerical and experimental methods to identify the dimensions of the BSSD components to eradicate the blood damage caused by the circulatory components. The proposed device design has been evaluated using computational fluid dynamics analysis for the blood damage caused due to the circulatory components of the BSSD by measuring the fluid shear stresses and their exposure time on the blood.

TABLE OF CONTENTS

LIST OF FIGURES

LIST OF TABLES

Chapter 1 Introduction

1.1 Cardiac Anatomy & Physiology

The heart is a muscular organ located between the lungs and slightly towards left of the center of the chest cavity. It is responsible for circulation of blood through the blood vessels of the body.

The heart is made up of a set of two pumps which consists of four chambers enclosed by thick, muscular walls. The upper two chambers are called the atria and the lower two chambers are called the ventricles. The right side of the heart provides blood to the systemic circulation loop.

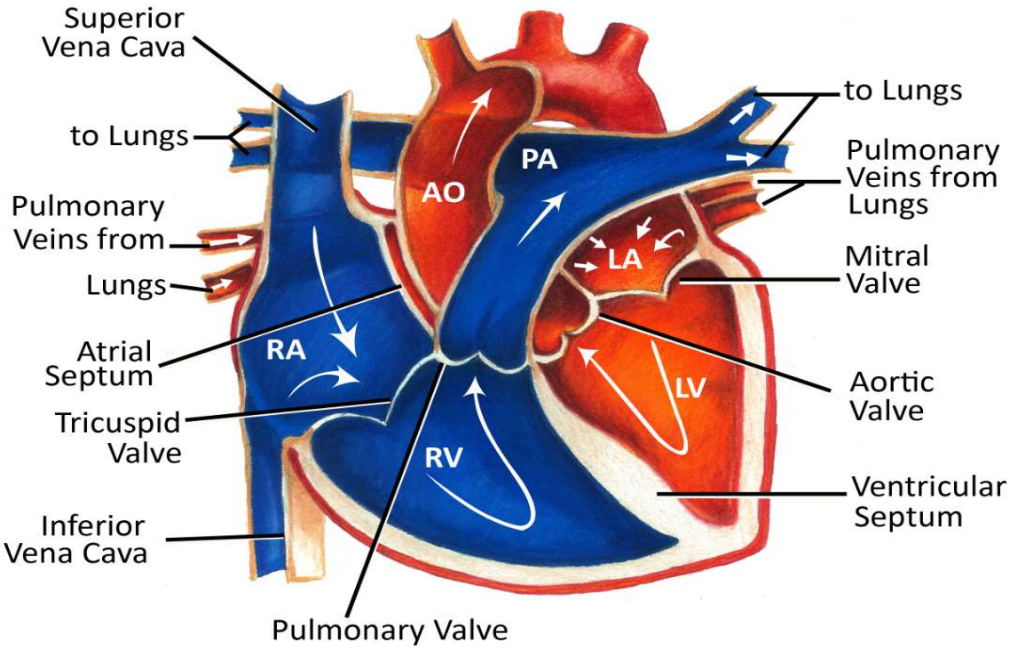

Figure 1-1 Anatomy of a Native Human Heart [1]

In the pulmonary circulation loop, the right atrium receives deoxygenated blood from the body through veins, known as vena cava. The right atrium then passes the blood to the right ventricle through a valve. This deoxygenated blood from the right ventricle is then pumped to the lungs via pulmonary artery, where it is oxygenated. The left atrium receives the re-oxygenated blood from the lungs through pulmonary vein. The re-oxygenated blood is pumped from the left atrium to the left ventricle through a valve. The left ventricle then contracts to transfer the re-oxygenated blood through the valve into the aorta. The oxygen rich blood from the aorta is then circulated to the body, which forms the systemic circulation loop.

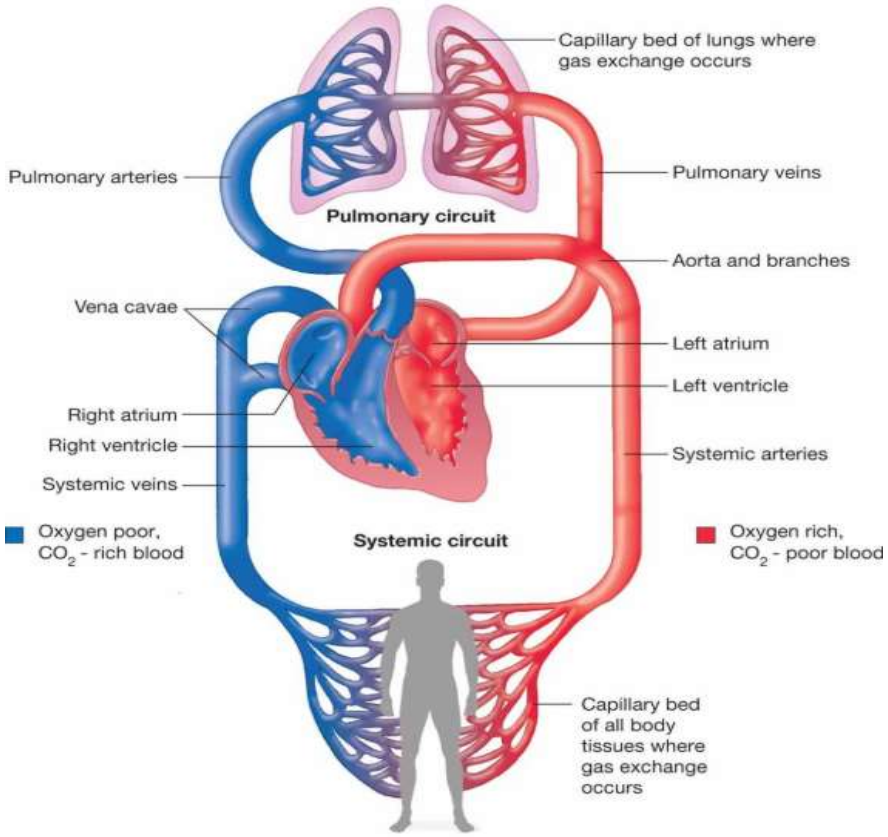

Figure 1-2 Pulmonary vs Systemic Circulation Loop [2]

The heart has four valves which enable the forward flow of the blood and prevent the backward flow by opening and closing the flaps once respectively during each heartbeat. The tricuspid valve is located between the right atrium and the right ventricle, and the mitral valve is between the left atrium and the left ventricle. The pulmonary valve is between the right ventricle and the pulmonary artery, whereas the aortic valve is situated between the left ventricle and the aorta.

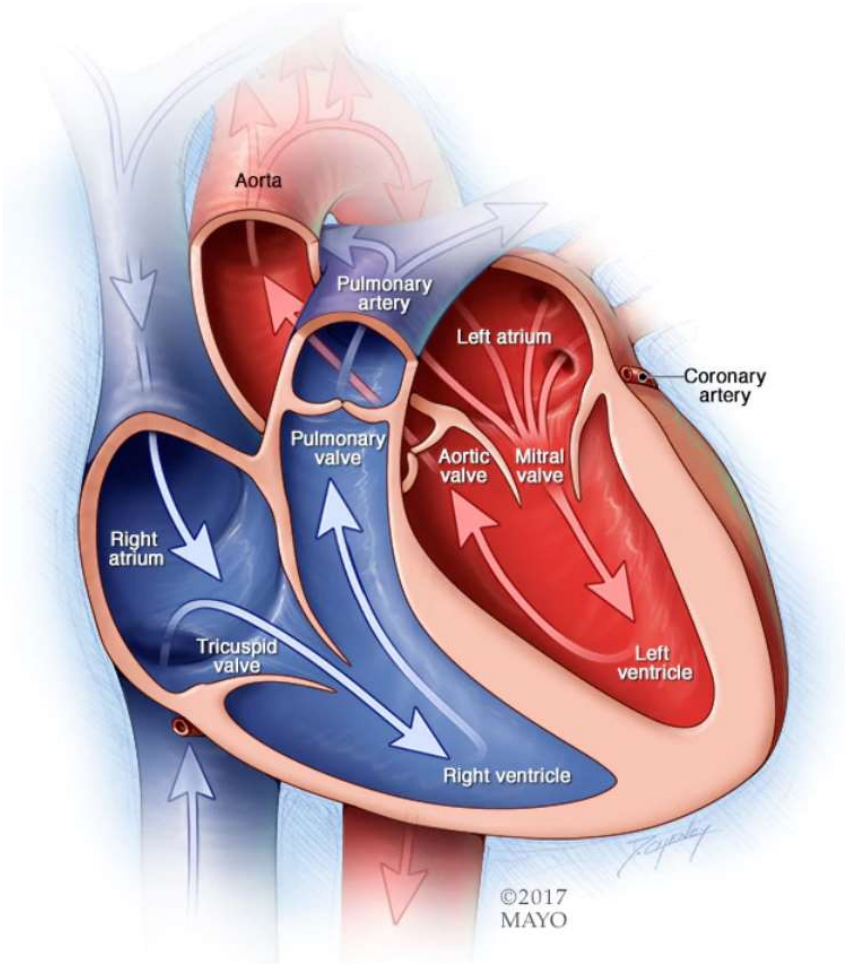

Figure 1-3 Chambers and Valves of Native Heart[3]

1.2 Congestive Heart Failure

Congestive Heart Failure (CHF), also known as heart failure (HF) is the leading cause of death in the United States. It can affect both children and adults. According to the Centers for Disease Control and Prevention, about half of the people who develop congestive heart failure die within five years of diagnosis [12].

Congestive Heart Failure is defined as the inability of the heart muscle to pump an adequate amount of blood to meet the body's needs. The common symptoms for CHF include shortness of breath, fatigue and weight gain. Medical conditions such as narrowed arteries in the heart, high blood pressure, and diabetes, slowly weaken the heart's ability to fill and pump blood through the body efficiently.

1.2.1 Types of Heart Failure

HF can be classified into different categories depending on the HF affected region location, pumping ability and the development of the disease [4]

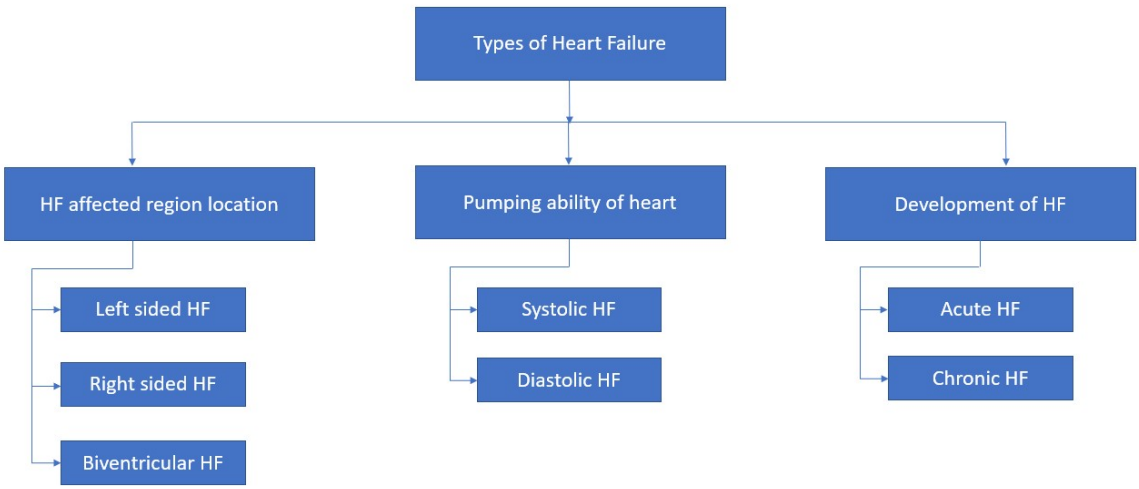

Figure 1-4 Classification of Heart Failure

1.2.1.1 Classification based on HF affected region location

Sometimes HF affects either the left side or the right side of the heart but can affect both sides. Depending on the location of the affected region, HF can be categorized as follows:

1.2.1.1.1 Left Sided Heart Failure

Left sided Heart Failure is the most common type of HF failure. It can be defined as the altered left ventricle function to pump oxygenated blood to the body efficiently. As a result, the blood accumulates in the lungs causing shortness of breath and fluid buildup.

1.2.1.1.2 Right Sided Heart Failure

Right sided Heart Failure is usually caused by Left sided HF. Due to the accumulation of blood in the lungs, the right atrium of the heart has to work harder to pump deoxygenated blood to the lungs which can result in its failure. This causes swelling in the legs, ankles and within the abdomen.

1.2.1.1.3 Biventricular Heart Failure

Biventricular Heart Failure can be defined when both the sides of the heart are affected. It can be considered as a combination of Left sided HF and Right sided HF. This can cause shortness of breath and swelling in the legs, ankles.

1.2.1.2 Classification based on pumping ability

HF can be classified in two types based on the pumping ability of the heart in order to help determine suitable medication and/or interventional procedures. The pumping ability of the heart is indicated using the concept of ejection fraction.

Ejection fraction (EF) is defined as the percentage of the blood leaving the heart though the left ventricle with each contraction. A healthy native heart's ejection fraction is between 55 and 70 percent [5].

1.2.1.2.1 Systolic Heart Failure

Systolic Heart Failure develops when the left ventricle of the heart cannot contract completely due to the weakened and enlarged heart muscle. This reduces the amount of blood pumped out of the heart into the body, resulting in reduced ejection fraction. An EF lower than 40 percent may be the evidence of systolic HF [6]. Systolic HF is also known as Heart Failure with reduced Ejection Fraction (HFrEF).

1.2.1.2.2 Diastolic Heart Failure

Diastolic Heart Failure develops when the left ventricle of the heart cannot relax between the heartbeats due to the stiff heart muscle. This results in inadequate filling of the blood in the heart. An EF higher than 75 percent may indicate a diastolic HF [6]. Diastolic HF is also known as Heart Failure with preserved Ejection Fraction (HFpEF).

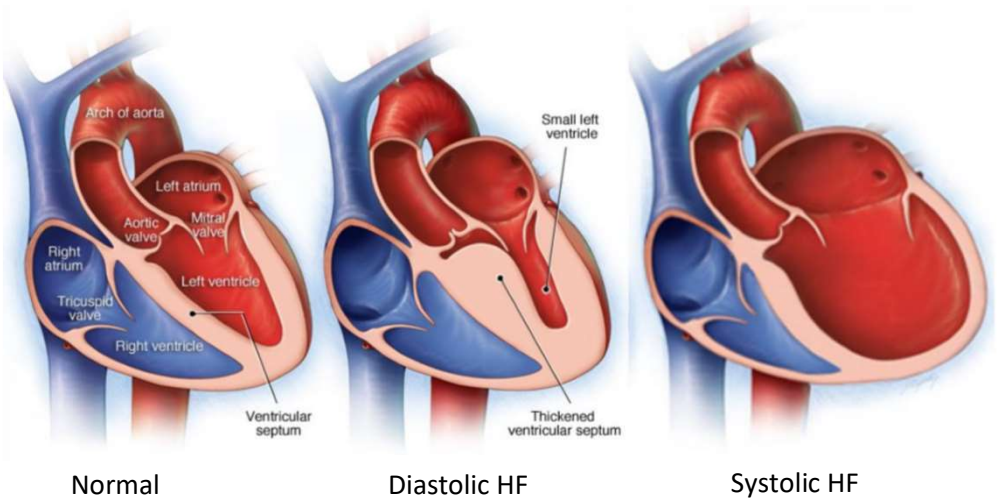

Figure 1-5 A comparison of a healthy heart to a heart with diastolic heart failure and a heart with systolic heart failure [7-8]

1.2.1.3 Classification based on the development of HF

HF can be categorized in two types based on its development as follows:

1.2.1.3.1 Acute Heart Failure

Acute Heart Failure develops suddenly as a consequence of heart failure, or other heart related problems. The symptoms are severe initially.

1.2.1.3.2 Chronic Heart Failure

Chronic Heart Failure develops gradually over time due to medical conditions like high blood pressure. The symptoms appear slowly and get worse with time.

1.2.2 Treatment of Heart Failure

The possible treatments for CHF vary with the severity of the patients' symptoms. The New York Heart Association (NYHA) classifies the HF patients in four classes based on the patient symptoms and objective assessment [9]. Table 1-1 describes the patient symptoms, and Table 1-2 describes the objective assessment.

Table 1-1 New York Heart Association classification of heart failure by patient symptoms

Class	Patient Symptoms
I	No limitation of physical activity. Ordinary physical activity does not cause undue fatigue, palpitation, dyspnea (shortness of breath).
II	Slight limitation of physical activity. Comfortable at rest. Ordinary physical activity results in fatigue, palpitation, dyspnea (shortness of breath).
III	Marked limitation of physical activity. Comfortable at rest. Less than ordinary activity causes fatigue, palpitation, or dyspnea.
IV	Unable to carry on any physical activity without discomfort. Symptoms of heart failure at rest. If any physical activity is undertaken, discomfort increases.

Table 1-2 New York Heart Association classification of heart failure based on objective assessment

Class	Objective Assessment
A	No objective evidence of cardiovascular disease. No symptoms and no limitation in ordinary physical activity.
B	Objective evidence of minimal cardiovascular disease. Mild symptoms and slight limitation during ordinary activity. Comfortable at rest.
C	Objective evidence of moderately severe cardiovascular disease. Marked limitation in activity due to symptoms, even during less-than-ordinary activity. Comfortable only at rest.
D	Objective evidence of severe cardiovascular disease. Severe limitations. Experiences symptoms even while at rest.

Mild CHF can be identified when the EF lies between 35 to 39 percent, and the pumping ability of the heart is moderately below normal [13]. The symptoms for mild CHF can often be alleviated by adopting an active lifestyle, a healthy diet and an appropriate exercise program. Various pharmacological therapies like Angiotensin-Converting Enzyme (ACE) Inhibitors, Angiotensin II Receptor Blockers (Beta Blockers or Inhibitors), Diuretics, Anticoagulants, Cholesterol-lowering drugs (statins), etc. can be prescribed to treat different symptoms or contributing factors of mild CHF depending on the patients' need [14].

For moderate to severe CHF, the pumping ability of the heart is significantly below normal, and the EF is below 35 percent [13]. The best treatment option in such cases is often a heart transplant [13]. However, despite a patient population of 6.4 million in the

US suffering from CHF, only about 2,500 heart transplants take place in the US each year, mainly due to the very low number of healthy human hearts available for transplant [16]. Mechanical circulatory support. (MCS) is available as a treatment option to augment cardiac function in patients while they wait for a donor heart to become available.

1.3 Mechanical Circulatory Support Devices

Mechanical Circulatory Support (MCS) devices are implantable mechanical devices, usually implantable pumps, which can either partially or completely replace the function of a failing heart. MCS devices are usually implanted as a Bridge to Transplant (BTT) – temporary use of the mechanical pump until transplant is available and a Destination Therapy (DT) – permanent pump implantation to aid the patients with end stage HF, after the exhaustion of pharmacological and conventional surgical therapies.

1.3.1 Classification of MCS devices

MCS devices can be categorized several different ways:

1.3.1.1 Pulsatile vs Continuous Flow MCS devices

Pulsatile MCS devices mimic the natural pulsing action of the heart. These devices use positive displacement pumps which need external drivers (pneumatic, hydraulic or electric) to provide alternating pressure and vacuum to fill and empty the pump chambers. Despite maintaining the physiological nature of the blood flow, pulsatile MCS devices have limited lifetime and low reliability due to mechanical wear and tear [18].

Continuous flow MCS devices use either an axial pump or a centrifugal pump to provide a continuous output flow that increases the arterial blood flow and pressure. Continuous flow MCS devices are smaller and have proven to be more durable than

pulsatile MCS. Early versions of continuous flow MCS used solid bearings, however newer pumps use magnetic levitation (maglev) or hydrodynamic suspension of moving impellers.

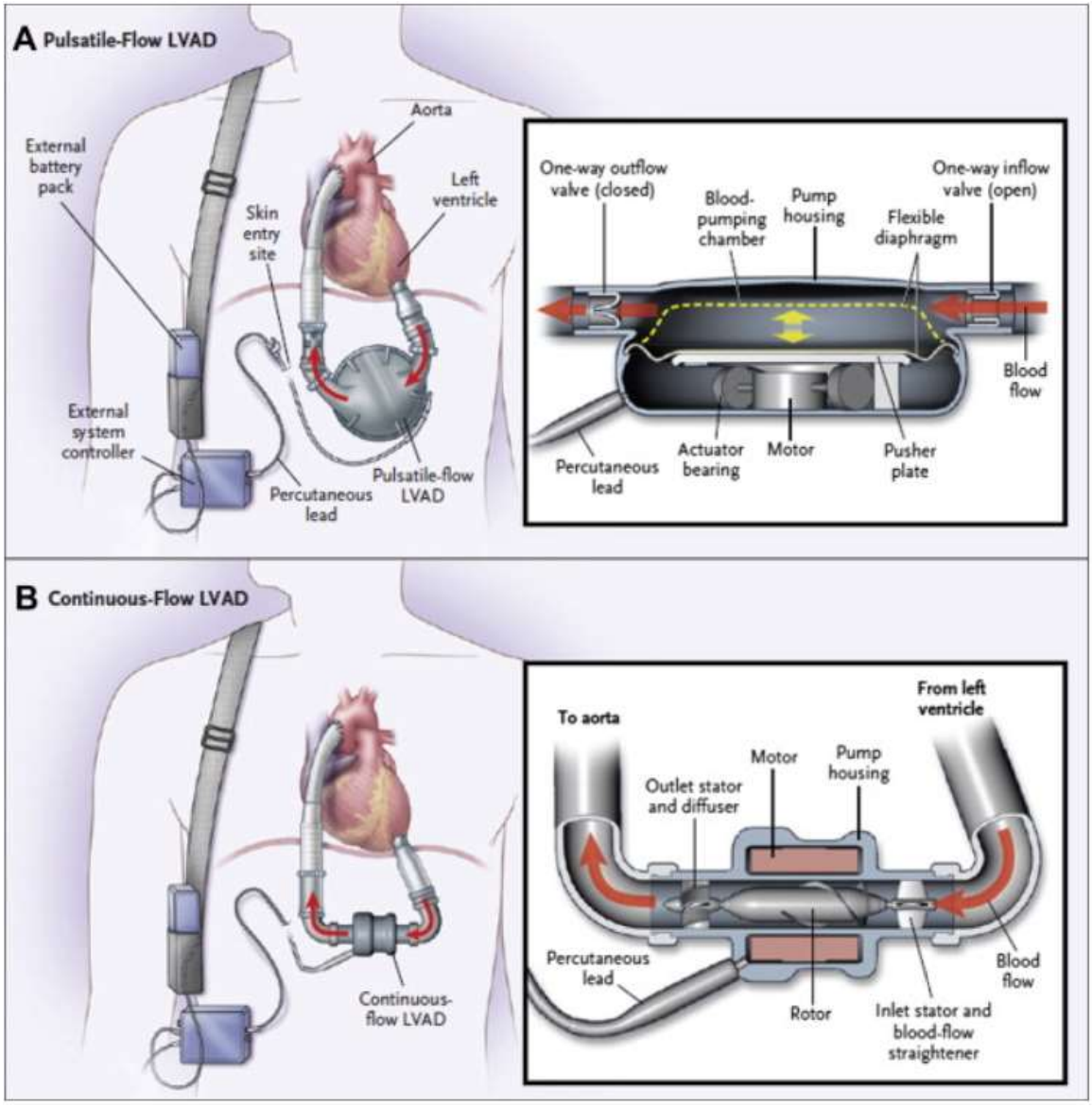

Figure 1-6 Pulsatile-flow MCS Support vs Continuous-flow MCS Support

1.3.1.2 Temporary vs Durable MCS devices

Temporary MCS devices are often implanted in HF patients as a bridge to decision (BTD) before receiving permanent or durable MCS devices. Temporary MCS devices can

provide support for days to weeks depending on the device mechanism. Current examples include the following.

The CentriMag® (Thoratec Corporation) is a surgically implanted centrifugal pump that can provide up to 10 L/minute of blood flow (normal human blood flow rate is about 5 L/minute). It is a third-generation continuous flow pump with a magnetically suspended rotor, which minimizes friction, thus reducing shear forces on red blood cells which can lead to hemolysis (destruction of red blood cells). The CentriMag system is currently Food and Drug Administration (FDA) approved (mandatory for the us in the U.S) for LV support up to six hours. It is approved for support when there is acute right ventricular (RV) failure for up to 30 days (Humanitarian Use Device), and longer-term use is currently investigational only [20].

Figure 1-7 CentriMag (Abbott)

The Impella® 2.5 system (Abiomed) is a 3 mm catheter-mounted, 2.5 L/minute, impeller-driven, axial-flow pump that is placed in a retrograde fashion across the aortic valve via a cardiac catheterization procedure. These devices can be inserted for short-term support, typically up to five days. [20]

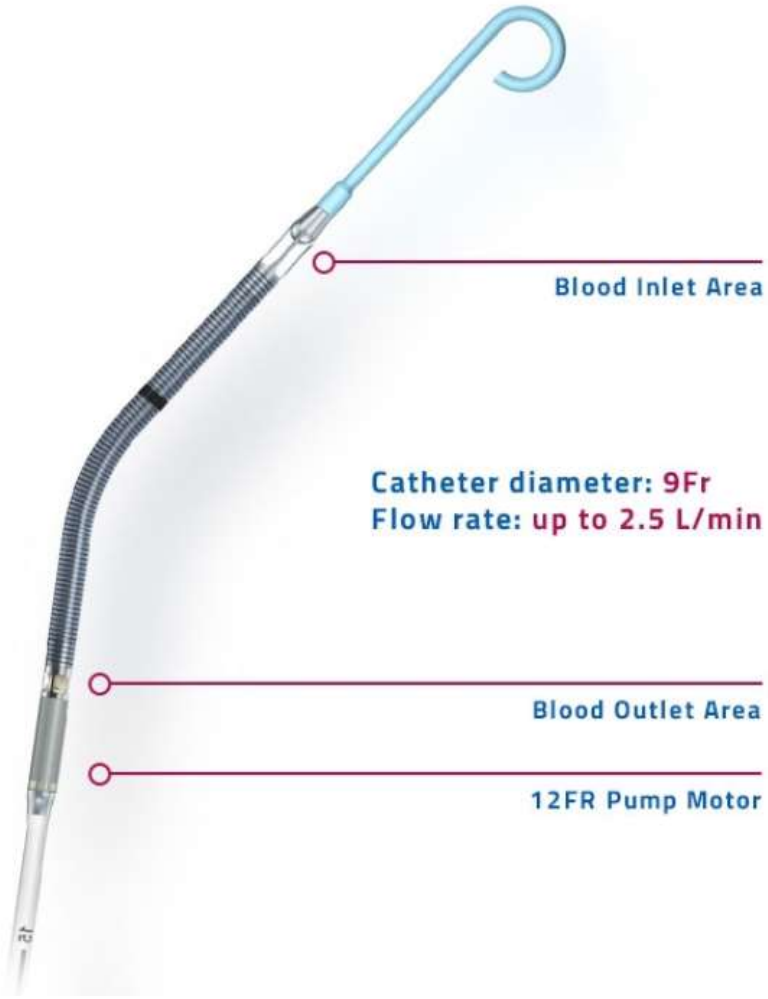

Figure 1-8 Impella 2.5 system (Abiomed)

Permanent or durable MCS devices include the Heartmate II (Abbot) Left Ventricular Assist Device (LVAD) which is designed to provide long-term circulatory support to intermediate-to-chronic heart failure patients. Its small, quiet pump features a

simple design with only one moving part and can provide blood flow equivalent to that of a healthy heart.

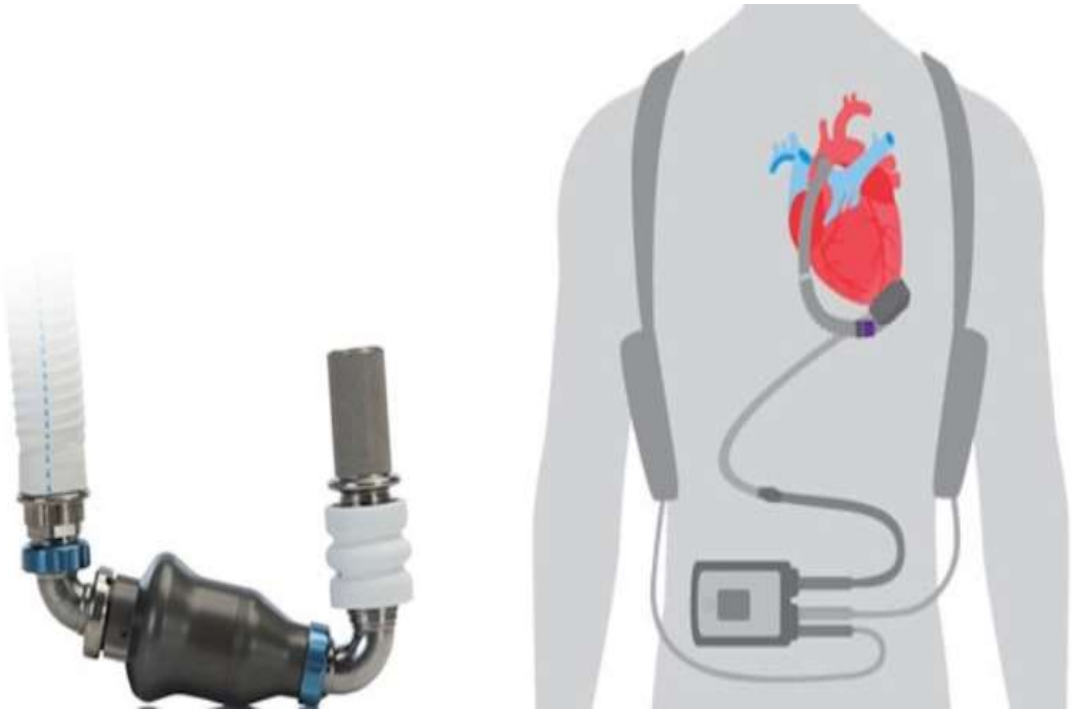

Figure 1-9 HeartMate II LVAD (Abbott)

1.3.1.3 Intracorporeal Vs Extracorporeal

Intracorporeal MCS devices are implanted within the human body which includes the permanent or durable MCS devices. Extracorporeal MCS devices are placed outside the human body to support the cardiac function usually for short term.

1.3.1.4 Ventricular Assist Device vs Total Artificial Heart

MCS devices are commonly classified into Ventricular Assist Devices (VAD) and Total Artificial Hearts (TAH) for long term care of end stage HF patients.

VADs are implantable, electromechanical devices attached directly to the patient's heart to augment the cardiac circulation. VADs are designed to assist either the left

ventricle (LVAD), the right ventricle (RVAD), or both ventricles (BiVAD). The Left Ventricular Assist Device (LVAD) is currently the most commonly used VAD to assist HF patients.

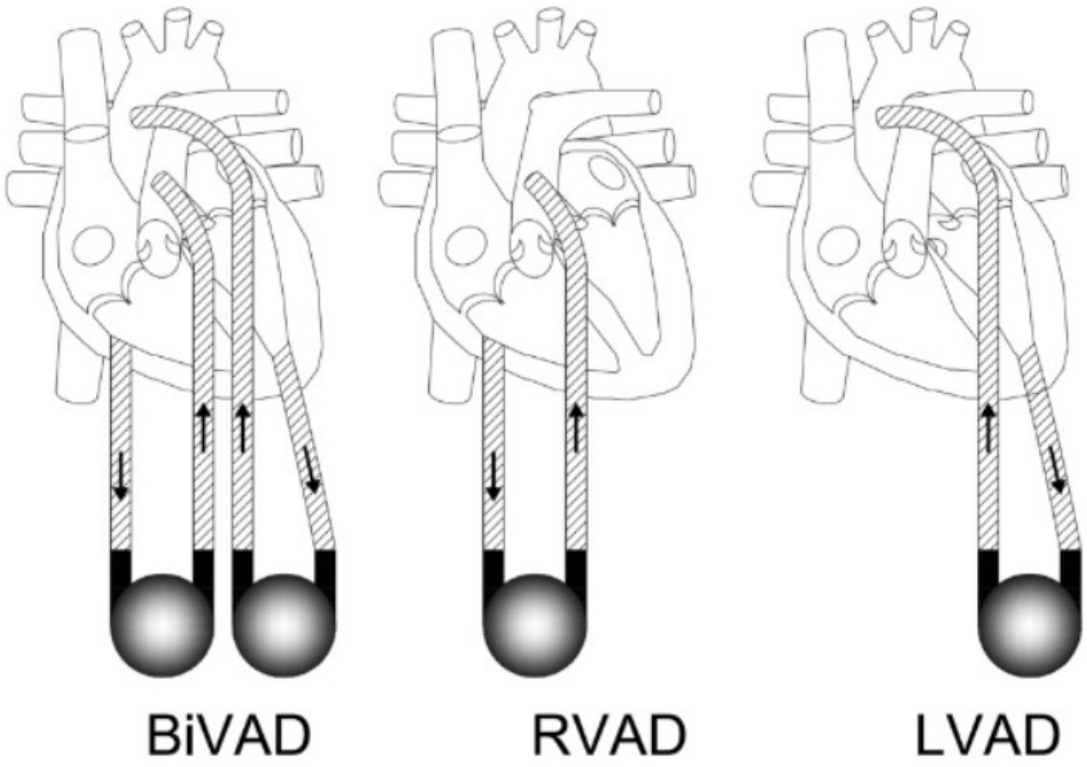

Figure 1-10 A schematic drawing of BiVAD, RVAD and LVAD

The TAH is an implantable device that replaces both the right and left ventricles, as well as the four heart valves, and occupies the space of the surgically removed, failing human heart. The TAH is used in patients with end-stage heart failure affecting both sides of the heart.

Figure 1-11 AbioMed Total Artificial Heart

1.3.2 Left Ventricular Assist Devices

Early research into LVADs was conducted primarily in the 1970s following recognition of the challenges associated with the TAH first implanted in 1969 [22].

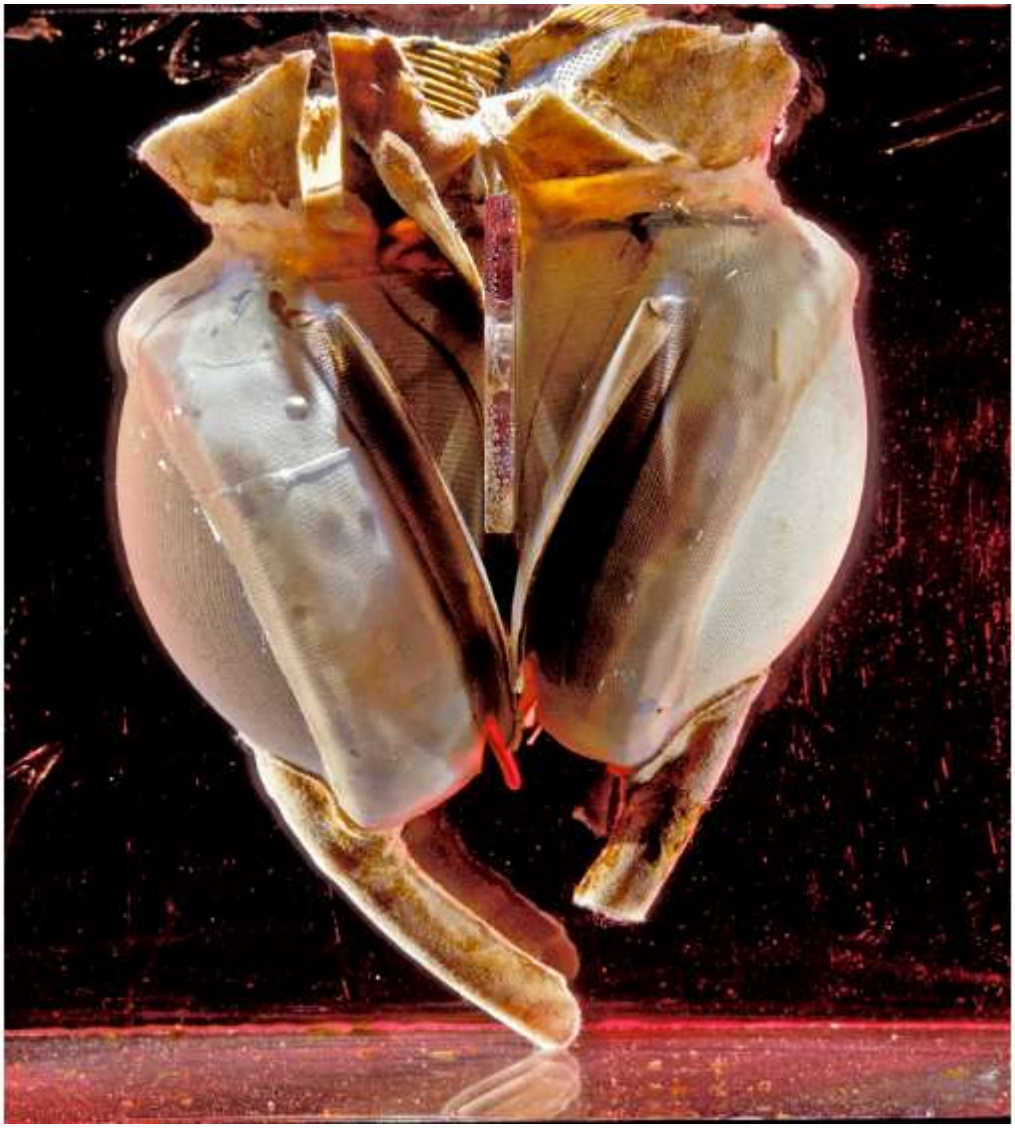

Figure 1-12 Liotta-Cooley first total artificial heart

The first generation LVADs were designed to replicate the native heart cardiac cycle and generate pulsatile flow using diaphragm and unidirectional artificial heart valve [19]. These bulky pulsatile LVADs were driven with an external drive either pneumatic or electric, which limited the patient's mobility. The very first successful implantation of a LVAD was completed by Dr. De Bakey in 1966 at Texas Medical Center, Houston to a 37-year old patient for ten days until her heart transplantation.[22] The first LVAD consisted of a titanium frame, a polyurethane pump.[21]and was driven pneumatically. The first

generation LVADs were improved with creation of Novacor LVADS (Baxter Healthcare, Oakland, CA, USA), HeartMate I (Thoratec), and Thoratec PVAD (Thoratec) [21] However, these devices proved incapable of long-term reliable performance due to the mechanical wear on the deformable membranes, short battery life and fatal surgically related complications.

Figure 1-13 First generation LVAD: HeartMate I (Thoratec) and Thoratec PVAD

The need to address the issues causing the failure of the first generation pulsatile LVADs stimulated the development of the second generation of LVADs involving the use of continuous flow pump. The Hemopump and the Jarvik 2000 developed by Dr. Wampler and Dr. Jarvik respectively at Texas Heart Institute (Houston, TX), laid the basis for the first clinical application of implantable continuous flow LVADs. With the development of the Hemopump, Dr. Wampler proved that high rotational speed pumps required to produce adequate flow could be designed to cause minimal damage to the red blood cells and the circulatory system. Similarly, the Jarvik 2000 marked the first use of nonlubricated, blood-washed bearings in a long-term implantable LVAD [26].

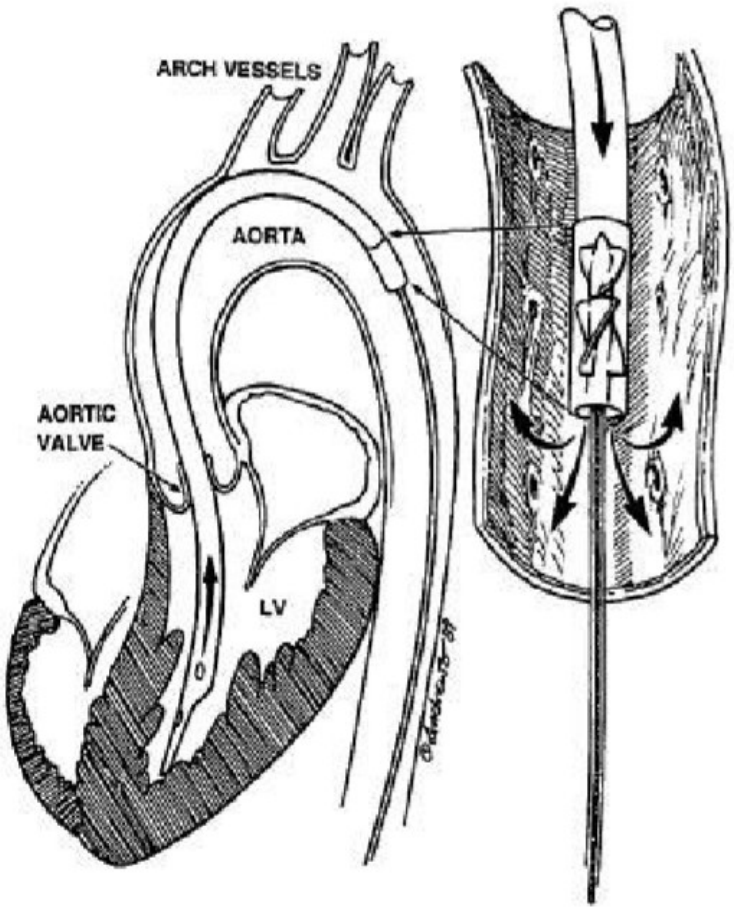

Figure 1-14 Hemopump

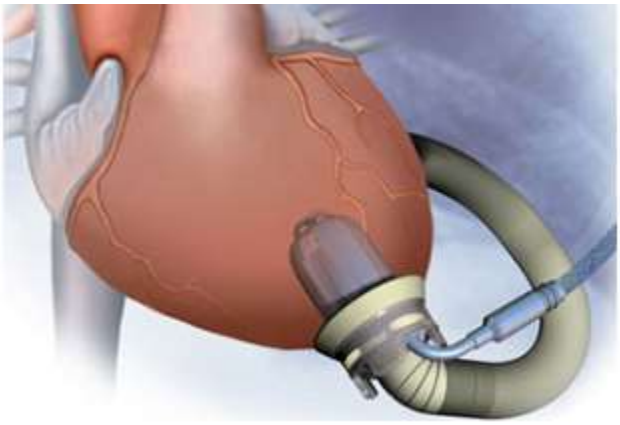

Figure 1-15 Jarvik 2000

The most frequently used second generation LVAD is the Heartmate II (Thoratec, Pleasanton, CA, USA). The device consists of an impeller surrounded by a metal case (the pump housing). The combined mechanical and magnetic positioning of the impeller increases the durability up to a minimum of five years [20].

Figure 1-16 HeartMate II (Thoratec Corporation)

The third generation LVADs achieved significant reduction in size. A centrifugal-flow LVAD, the HeartWare (HeartWare International, Inc., Framingham, MA, USA), has a smaller, more flexible driveline and does not need a pump pocket. Designed as a radial pump with magnetic and hydraulic positioning, the third generation LVAD has an estimated durability of 10 years. The HeartMate III Left Ventricular Assist System (Abbott) is a completely bearing-less pump that is now FDA approved and is in widespread clinical use.

Figure 1-17 Heartmate III

Figure 1-18 Heartware HVAD

Despite decades of innovations that have led to more than 40,000 implants of clinical LVADs, there are still complications to be addressed.

1.3.2.1 LVAD Complications

Major LVAD complications fall into two categories related to surgical procedure and device design. Surgical complications include infection and internal bleeding whereas device design complications revolve around hemocompatibility.

1.3.2.1.1 Hemocompatibility

Hemocompatibility is defined as a measure of the physiological response induced by an implanted device when in contact with blood.[52] It is very important to assess the hemocompatibility of a LVAD design to ensure successful clinical functioning of the device, minimizing cost and maximizing the pump efficiency.

Blood is made of four important components:

- Plasma: The liquid component of blood is called plasma, a mixture of water, sugar, fat, protein, and salts. The main job of the plasma is to transport blood cells throughout the body along with nutrients, waste products, antibodies, clotting proteins, chemical messengers such as hormones, and proteins that help maintain the body's fluid balance.
- Red Blood Cells (RBC): Red Blood Cells, also known as erythrocytes, are the most abundant cell in the blood, accounting for about 40 to 45 percent of its volume. The shape of a red blood cell is a biconcave disk with a flattened center. RBCs contain a protein called hemoglobin, which helps carry oxygen from the lungs to the rest of the body and then returns carbon dioxide from the body to the lungs so it can be exhaled.

- White Blood Cells (WBC): White Blood Cells, also known as leukocytes, protect the body from infection. They are much fewer in number than RBC, accounting for about 1 percent of blood.
- Platelets: Platelets, also known as thrombocytes, are small fragments of cells. Platelets help the blood clotting process (or coagulation) by gathering at the site of an injury, sticking to the lining of the injured blood vessel, and forming a platform on which blood coagulation can occur. This results in the formation of a fibrin clot, which covers the wound and prevents blood from leaking out. Fibrin also forms the initial scaffolding upon which new tissue forms, thus promoting healing.

Within an implanted LVAD, the blood is exposed to non-physiological mechanical stresses which may lead to blood damage, and possibly pump failure. The mechanical stresses are generated due to the circulatory components of the pump rotating at high speeds, which could create either a low shear stress regime or a high shear stress regime.

In a low shear stress region, thrombosis, or pathologic clotting of the blood, can occur and inhibit the blood flow through the circulatory system. Conversely, a high shear stress regime can cause destruction of red blood cells leading to the release of hemoglobin into the bloodstream, termed hemolysis.

1.4 Intra-Atrial LVAD

An experimental intra-atrial pump (IAP) is under development at Texas Heart Institute. It is comprised of a pumping system, a bearing system, and a motor system. An unpublished evaluation of the hemocompatibility of the IAP has detected the presence of hemolysis, though the precise source has yet to be identified.[60-64]

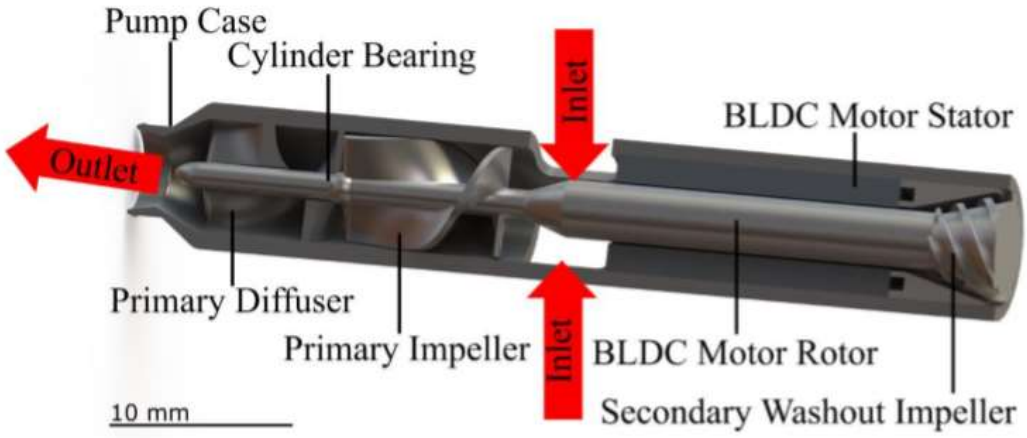

Figure 1-19 Cross-section of the intra-atrial pump design

Figure 1-20 Intra-Atrial Pump Assembly (Texas Heart Institite, Houston, TX)

1.5 Motivation for Blood Shear Stress Device

Study of hemolysis and the blood damage using computational as well as experimental methods has been an area of interest for the researchers since a long time [49-59]. Couette type blood shearing device, using bearings [70] calculated the hemolysis index by experimental and numerical studies. We propose a blood shear stress device (BSSD) to isolate each component of the LVAD to enable hemolysis testing and identify the source.

This thesis describes the steps taken towards the development of a BSSD. Firstly, it elaborates on the features and functions of the BSSD, including the sub-systems. Numerical techniques were employed to evaluate the magnetic bearing system and motor system; these results were validated by experiment methods. Lastly, Computational Fluid Dynamics analysis was performed using numerical methods to calculate the inherent hemolysis in the Blood Shear Stress Device (BSSD).

Chapter 2 Blood Shear Stress Device: Design Proposal

The preliminary design of the Blood Shear Stress Device (BSSD) proposed in this thesis operates on a short blood exposure time, a loop for repeated blood exposure, and no sealing fluid to accurately study shear stress' impact on blood trauma levels. BSSD will test three individual components of the intra-atrial pump namely (1) primary impeller, (2) motor gap and (3) secondary washout impeller to identify specific sources of blood trauma, allowing rapid iteration and refinement of pump components.

In order to serve as a platform to evaluate the hemocompatibility of the pump, the BSSD should not induce hemolysis inherently. Thus, this device deploys brushless direct current (BLDC) motor along with magnetic levitated (maglev) bearing systems to eliminate significant blood damage caused due to contact bearings [31] and ensure continuous blood flow within. BSSD described here will be the first blood shearing device using maglev to eliminate contact points to be reported in the literature. The BSSD includes an exchangeable rotor feature for individual component study of the LVAD.

2.1 Sub-Systems

The blood shear stress device incorporates three sub systems to aid in LVAD component testing and identification of sources of blood trauma. These sub-systems are described as follows:

2.1.1 Passive Magnetic Levitation System

The passive maglev system uses two ring-shaped permanent magnets fixed to the rotor shaft and two ring-shaped permanent magnets attached to the stator. The BLDC motor is responsible for the rotation, θ_z whereas the permanent magnetic rings passively stabilize

the radial translation in x and y direction, and inclination of each axis θ_x and θ_y respectively.

2.1.2 Active Magnetic Levitation System

In the active maglev system, all the passive permanent magnet rings are magnetized axially to stabilize the z direction.

The Maglev Bearing System uses both active maglev system and passive maglev system to provide stability for all the six degrees of freedom.

2.1.3 Testing System

The testing system includes an exchangeable rotor and a stationary stator attached to maglev bearing system. The exchangeable rotor enables testing for components of LVAD as well as for a wide range of dimensions, and sterilization between tests to prevent bacteria-induced blood trauma. The stationary component can be exchanged to match either the dimensions of the motor stator for testing motor gaps, or the dimensions of the pump housing when evaluating impeller hemolysis.

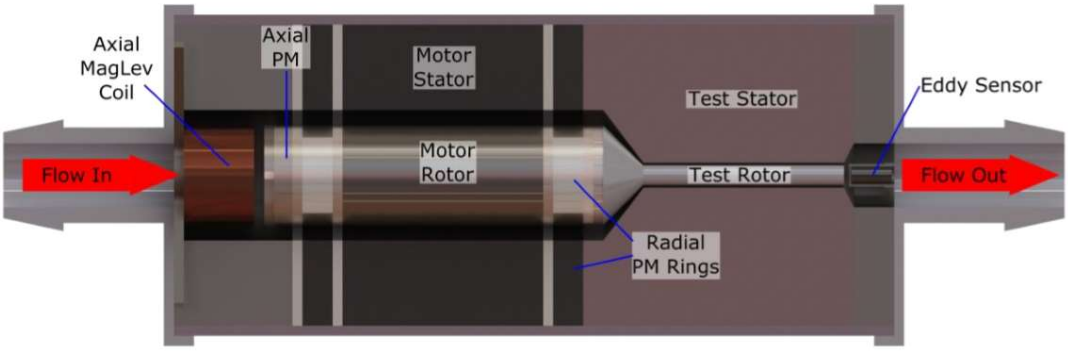

Figure 2-1 A schematic diagram of a blood shear stress device with exchangeable parts and magnetically levitated motor

Chapter 3 Modeling Passive Magnetic Levitation

Magnetic Levitation can be defined as a method to suspend loads using magnetic fields. Magnetic bearings utilize the maglev technology to support moving parts, translational or rotational, without any physical contact. In case of a motor, a magnetic bearing can levitate a rotating shaft and permit relative motion with very low friction and no mechanical wear. Magnetic bearings support the highest speeds and have no maximum relative speed. The use of magnetic bearings offers very low and predictable friction, and the ability to run without lubrication and in a vacuum.

Magnetic bearings are widely used in industrial machines such as compressors, turbines, pumps, motors and generators. Due to their ability to eliminate contact points, and thereby reducing thrombosis and extending device longevity, the use of magnetic bearings in total artificial hearts and ventricular assist devices has gained immense popularity/acceptance/demand. Several blood pumps already have utilized magnetic bearings clinically.

It was presented by Earnshaw in 1842 that a static magnetic field, using permanent magnets or electromagnets being supplied with a constant current, cannot achieve stable magnetic levitation. Therefore, in order to control the six degrees of freedom of the rotor with maglev technology, it is effective to combine active and passive bearings [36-37].

Reducing the number of actively controlled axes minimizes the number of sensors and electronics needed, thereby shrinking the device and improving reliability [36] HeartMate 3 (Thoratec Corp.) employs a radial bearing-less motor, actively controls rotor rotation and two degrees of freedom radially, and passively stabilizes the axial translation

and inclination. Incor (Berlin Heart GmbH) uses a radial gap motor to rotate the rotor, and axial magnetic bearings to control axial displacement. It also employs passive stabilization to control radial translation and tilt. BiVACOR (BiVACOR Inc.) [33] has an axial gap motor and axial magnetic bearings. The axial magnetic bearings stabilize axial translation and inclination, while passive stability controls radial translation. The BSSD will employ active control in the axial direction, and passive control of radial position and inclination to minimize the number of control axes. Fewer control axes will decrease the outer diameter and the number of sensors and electronics needed.

3.1 Permanent Magnet Rings

The passive magnetic levitation system uses two concentric permanent magnet (PM) rings, inner rotating PM ring and outer stationary PM ring respectively, made up of the strongest permanent magnet available commercially, neodymium magnet.

A neodymium magnet (NdFeB) is a rare-earth magnet made from an alloy of neodymium, iron, and boron. Based on the manufacturing processes, they are divided into two subcategories, namely sintered NdFeB magnets and bonded NdFeB magnets. Sintered NdFeB magnets are prepared by the raw materials being melted in a furnace, cast into a mold and cooled to form ingots. The ingots are pulverized and milled; the powder is then sintered into dense blocks. The blocks are then heat-treated, cut to shape, surface treated and magnetized. Bonded NdFeB magnets are prepared by melt spinning a thin ribbon of the NdFeB alloy. This ribbon is then pulverized into particles, mixed with a polymer, and either compression- or injection-molded into bonded magnets.

Neodymium magnets are graded according to their maximum energy product, which relates to the magnetic flux output per unit volume. Higher values indicate stronger magnets.

The sintered NdFeB magnets values range from 28 up to 52. The first letter N before the values is short for neodymium, meaning sintered NdFeB magnets. Letters following the values indicate intrinsic coercivity and maximum operating temperatures. The temperature ratings available are - M - H - SH - UH - EH-AH.

Table 3-1 Classification of Neodymium Magnets with respect to the Maximum Operating Temperature

Neodymium Material Type	Maximum Operating Temperature	Curie Temperature
N	176°F (80°C)	590°F (310°C)
N-M	212°F (100°C)	644°F (340°C)
N-H	248°F (120°C)	644°F (340°C)
N-SH	302°F (150°C)	644°F (340°C)
N-UH	356°F (180°C)	662°F (350°C)
N-EH	392°F (200°C)	662°F (350°C)
N-AH	428°F (220°C)	662°F (350°C)

The curie temperature is the temperature at which the material loses its magnetism.

The concentric PM rings used in the passive magnetic levitation system evaluated in this research are sintered NdFeB magnets of N48H grade manufactured by Yantai Shougang Magnetic Materials Inc (Yantai, China). These PM rings offer a maximum energy product (BHmax) range of 44 to 49 MGOe (Mega – Gauss Oersted) and a maximum operating temperature of 120 Celsius.

The basic geometry of the PM rings with the three dimensions inner diameter (ID), outer diameter (OD) and length (L) is shown in the figure [3-1],

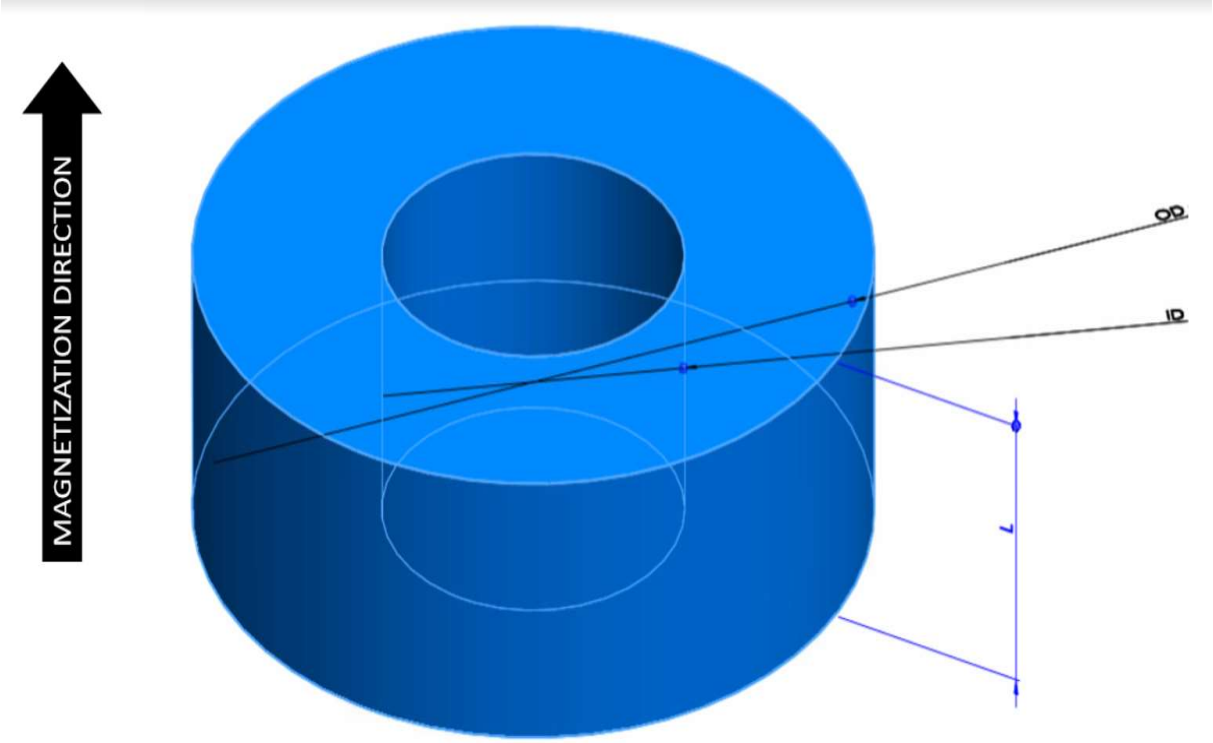

Figure 3-1 Basic geometry of a permanent magnet ring

This study evaluates 27 different geometries obtained by varying OD of the outer PM ring and OD of the inner PM for the length 1 mm, 2 mm and 3mm. The ID of the inner PM ring and the outer PM ring is set to 4 mm and 10.7 mm respectively. The table [3-2] lists the considered values for the length of the PM rings, OD of the inner PM ring and OD of the outer PM ring the numerical and the experimental study.

Table 3-2 List of values considered for the input variables for the numerical and experimental study of the PM rings

Sr No.	Length (mm)	Outer Diameter of Outer PM Ring (mm)	Outer Diameter of Inner PM Ring (mm)
1	1	16	6
2	2	18	8
3	3	20	10

3.1.1 Methods

This section explores the numerical and experimental methods to study the behavior of magnetic forces induced in the concentric PM rings due to axial and radial displacement of the inner PM ring. Section 3.1.1.1 discusses the finite element method using numerical simulation software COMSOL 5.4 for the axial and radial magnetic force evaluation in concentric PM rings with respect to the displacement. Section 3.1.1.2 elaborates the experimental methods to analyze twenty-seven geometries of varying inner and outer PM ring diameter and length using a custom-made test rig.

3.1.1.1 Numerical Methods

The components of the passive maglev system are evaluated using FEM in numerical simulation software COMSOL 5.4 to effectively design the magnetic bearings in order to stabilize the rotor of the BLDC motor radially in the BSSD.

A 3-dimensional geometry of inner PM ring concentrically placed inside the outer PM ring is designed in COMSOL 5.4. The ID of the outer PM ring and the inner PM ring

is set equal to that of the ID of the stator and the rotor of the BLDC motor to provide a clear blood flow pathway. Hence, the ID of the inner PM ring and the outer PM ring is fixed to 4 mm and 10.7 mm respectively.

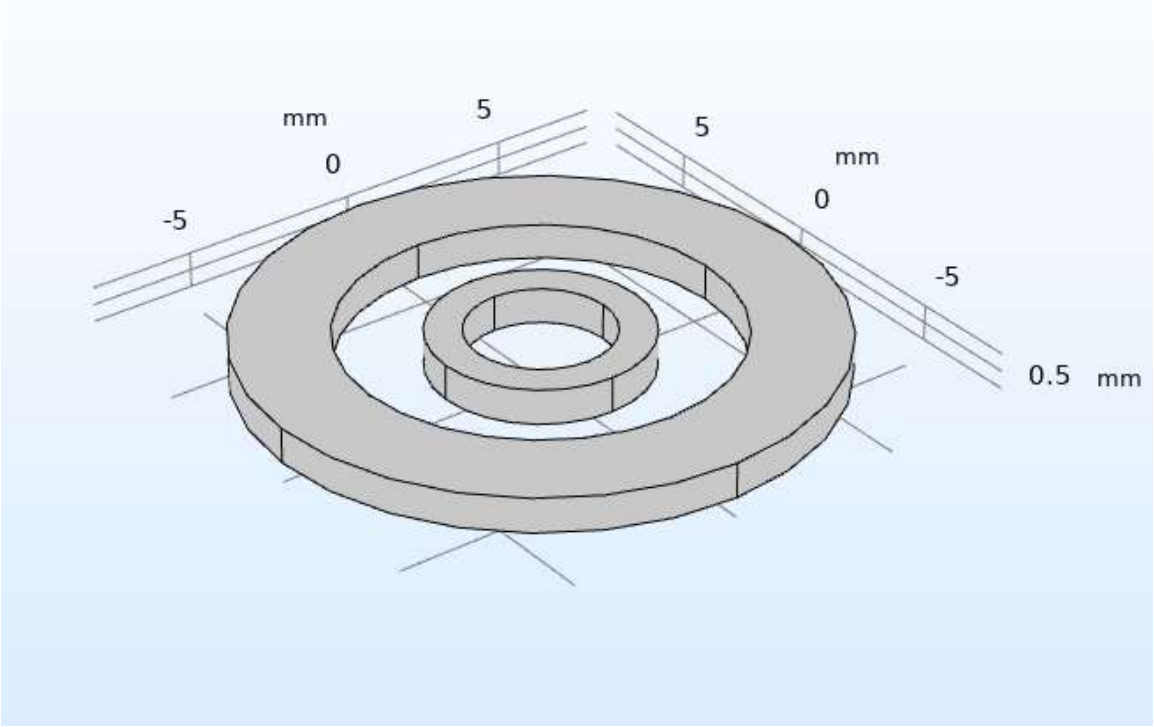

Figure 3-2 A 3D geometry of concentric PM rings in COMSOL 5.4

A user defined fine mesh is created using tetrahedrons with maximum and minimum element size of 0.2 mm and 0.1 mm respectively. The mesh is calibrated for general physics with maximum element growth rate of 1.3.

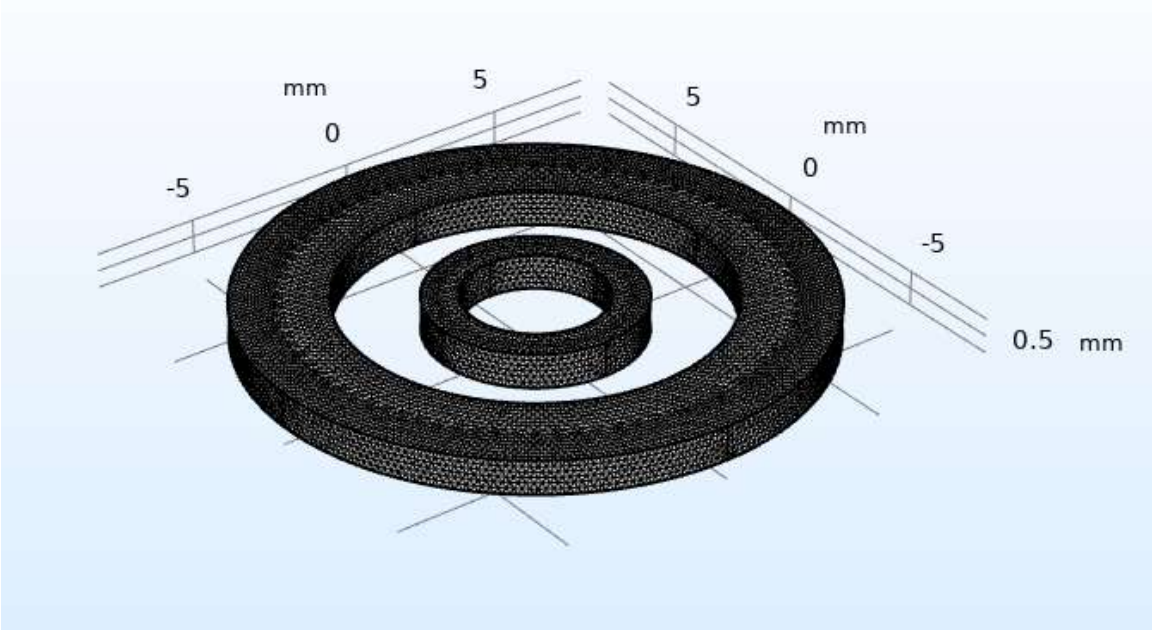

Figure 3-3 Generated Mesh for the concentric PM rings

A *Magnetic Fields, No Cur*rents interface is employed for this set of PM rings, which formulates this as a magnetostatic problem where no currents are involved. This interface uses the magnetic scalar potential, V_m with an initial value of zero to solve the concentric passive PM rings.

In a current free region [48],

$$\nabla \times H = 0 , \tag{3-1}$$

where H is the Magnetic Field Intensity, A/m

Equation (3-1) implies that the magnetic scalar potential, V_m can be defined from the relation,

$$H = -\nabla V_m, \tag{3-2}$$

which is analogous to the definition of the electric potential of the static electric fields.

Magnetic Flux conservation is applied to the inner and the outer PM ring where the magnetic field, B is calculated by

$$B = \mu_0 \mu_r H + B_r, \tag{3-3}$$

where $\mu_0$is the permeability of vacuum, 1.257e-06 H/m, μ_r is the relative permeability obtained from the material and B_r is the remanent flux density, 1.2 T.

The axial and radial forces calculated on the inner PM ring when it undergoes axial and radial displacement are governed by equation (3-4)

$$F = \oint nT \, dS. \tag{3-4}$$

A parametric sweep is used to independently vary the geometric parameters and displacement. The OD of the inner PM ring is varied from 6 to 10 mm, the OD of the outer PM ring from 16 to 20 mm, and length from 1 to 3 mm. The inner PM ring is displaced axially and radially from 0-1.0 mm with a 0.2 mm increment in the axial direction and 0.1 mm increment in the radial direction.

3.1.1.2 Experimental Methods

The experimental setup for the evaluation of the axial and the radial forces generated within the concentric PM rings with respect to the displacement in axial and radial direction involves a custom test rig made up of a non- magnetic material, aluminum.

Figure (3-2) shows the assembly of the custom test rig designed by Dr. P. Alex Smith, Research Engineer III using Solidworks at Center for Technology Innovation, Texas Heart Institute (Houston, TX).

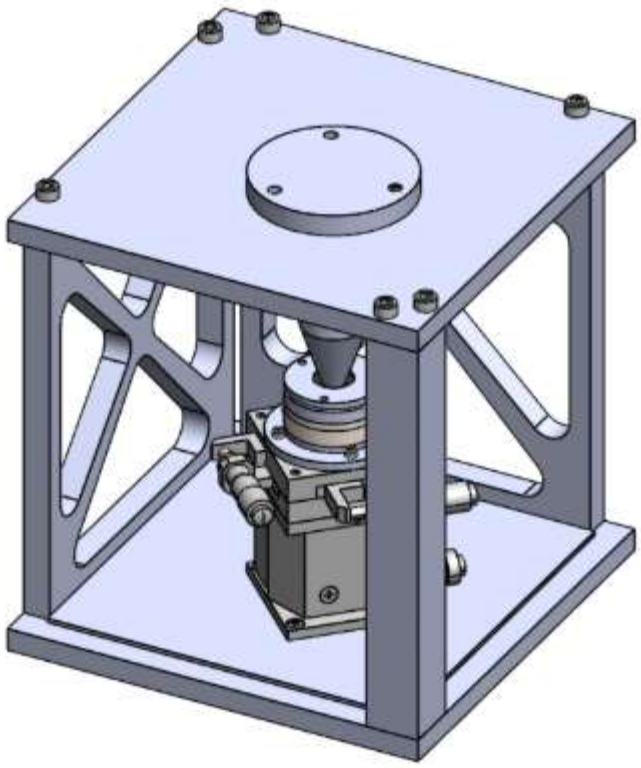

Figure 3-4 An assembly of manufactured test rig for magnetic force evaluation of the PM rings

In the test rig, the top plate and the base platform are supported by two vertical components namely side walls and brace. The inner PM ring holder is responsible for the alignment of the inner PM ring using brass shoulder screws. The outer PM ring holder and the PM ring retention hold the outer PM ring in position.

These components were manufactured at by Juan Fernandez, Lead Machinist at Houston Methodist Research Institute (Houston, TX). The magnetic force test rig was assembled at Center for Technology Innovation, Texas Heart Institute (Houston, TX). It uses a highly precision stainless-steel x-y-z stage ((XYSSG60 and ZLPGS60, MiSUMi Group, Inc., Tokyo, Japan) moved by a micrometer head for the axial and radial displacements in the z and x direction respectively. The outer PM ring is held in place by

outer PM ring holder and the PM ring retention, is mounted on a force transducer (Nano43, ATI Industrial Automation, Apex, NC, USA). The force transducer is mounted on the x-y-z stage. The inner PM ring holder is then mounted on the top plate with inner PM ring held in position. The outputs given by the force transducer using a Simulink code as a result of the displacements in z and x direction are acquired using by a dSpace MicroLabBox (DS1202, dSPACE Inc., Paderborn, Germany).

The first step towards the magnetic force testing on the test rig involves alignment of the axially polarized inner PM ring and the axially polarized outer PM ring such that this concentric arrangement is radially stable and axially unstable. The outer PM ring is then mounted on the force transducer using a PM ring holder and PM ring retention. This is followed by taring of the forces generated in the x, y and z direction due to weight of the outer PM ring. The inner PM ring is then placed concentrically with the outer PM ring using PM ring holder mounted on the top plate of the test rig. The center alignment of the inner PM ring with respect to the outer PM ring is achieved by adjusting the micrometer head until the forces in the x, y, z direction is null.

The inner PM ring is displaced axially using the micrometer head on the stage from 0 to 1 mm with an increment of 0.1 mm in z direction. The axial forces generated are recorded, and then the inner PM ring is brought to the initial centered position. The inner PM ring is then subjected to radial displacement with the help of micrometer gauge from 0 mm to 1 mm with 0.1 mm increment in in x direction. The generated radial forces are recorded, and the inner PM ring is brough to the initial position.

The above-mentioned testing process is performed twice for each of the 27 geometries of varying OD of the inner PM ring and the outer PM ring for lengths 1 mm to

3 mm. The results are used to calculate the axial and the radial stiffness to design the passive maglev bearing system for BLDC motor. The radial and axial stiffness of PM rings is calculated by equation [3-5, 3-6] [31].

$$k_{pm\_r} = \frac{F_{pm\_r}}{\Delta r} \; when \; \Delta z = 0 \;\; \text{and} \tag{3-5}$$

$$k_{pm\_z} = \frac{F_{pm\_z}}{\Delta z} \; when \; \Delta r = 0, \tag{3-6}$$

where F_{pm_r} and F_{pm_z} are the magnetic force generated by PM rings because of inner PM ring radial and axial displacements, Δr and Δz respectively, and k_{pm_r} and k_{pm_z} are the radial and axial stiffness coefficient.

3.1.2 Results

The numerical and experimental evaluation for 27 geometries obtained by varying OD of the inner PM ring, the OD of the outer PM ring and the length of the PM rings has been performed. This section describes the effect of (1) Change in OD of the inner PM ring, (2) Change in OD of the outer PM rings, and (3) Change in the length of the PM rings, on the axial and the radial stiffness with respect to the displacement.

3.1.2.1 Effect of change in OD of the inner PM ring

Three dimensions have been considered for the OD of the inner PM ring of the passive maglev system, namely, 6 mm, 8 mm, and 10 mm. As the OD of the inner PM ring increases, the concentric gap between the outer PM ring and the inner PM ring decreases.

When the inner PM ring is subjected to axial displacement from 0 mm (centered position) to 1 mm with 0.2 mm increment in axial direction, the axial stiffness of the 6 mm inner PM ring (length 1 mm) reduces by 7% with each increment, both numerically and

experimentally. There is an approximate reduction of 9% and 21% in the axial stiffness for the 8 mm inner PM ring (length 1 mm) and 10 mm inner PM ring (length 1 mm) respectively with 0.2 mm increment in the axial direction.

Increasing outer diameter of the inner PM ring from 6 mm to 10 mm results in 20-30% increase in axial stiffness numerically whereas 30% increase experimentally. These results are presented in the figure (3-3).

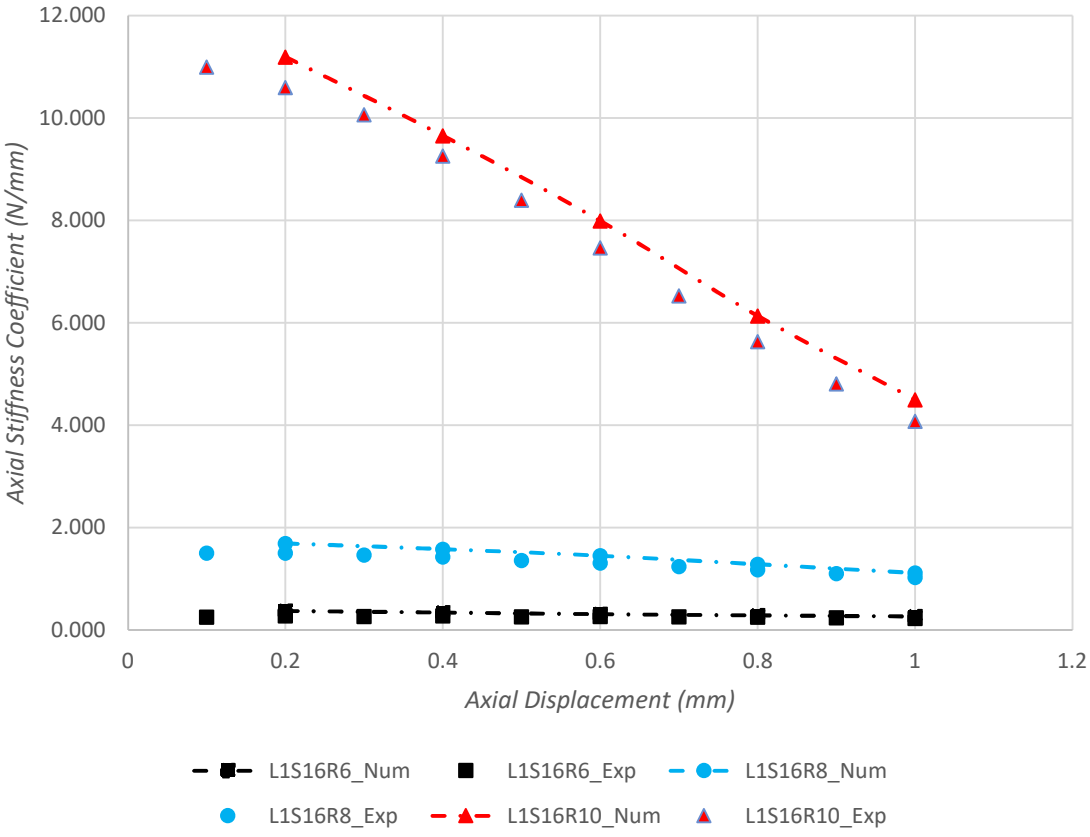

Figure 3-5 Change in Axial Stiffness Coefficient for different inner PM ring OD with respect to axial displacement

When the inner PM ring is radially displaced from 0 mm (centered position) to 1 mm with 0.1 mm increment in radial direction, the radial stiffness of the 6 mm inner PM ring (length 1 mm) increases by 2% approximately with each increment. There is an increase of around 3% and 4% in the radial stiffness for the 8 mm inner PM ring (length 1

mm) and 10 mm inner PM ring (length 1 mm) respectively with 0.1 mm increment in the radial direction.

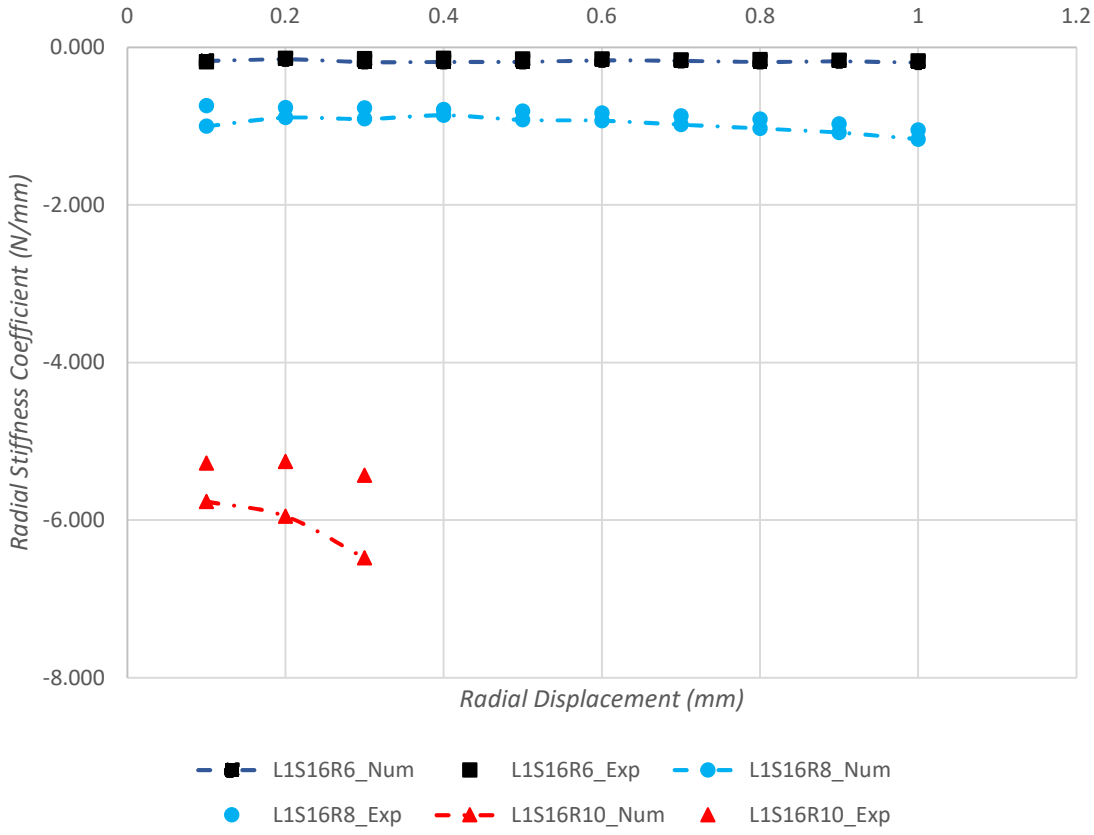

Figure 3-6 Change in Radial Stiffness Coefficient for different inner PM ring OD with respect to radial displacement

As seen from the plots, the numerical and experimental readings record an approximate increase of 35% in radial stiffness with the increase of OD of the inner PM ring from 6 mm to 10 mm. The figure (3-3) and (3-4) portray the effect of change in the OD of the inner PM ring. The length of the PM rings and the OD of the outer PM ring have separate effects on the axial and the radial stiffness with respect to the displacement.

3.1.2.2 Effect of change in the length of the PM rings

Lengths of 1 mm, 2 mm, and 3 mm have been evaluated using numerical and the experimental analysis of the concentric PM rings for the passive maglev system of the

BSSD. The effect of the length of the PM rings for the maximum and the minimum concentric gap of the PM rings assembly have been discussed in this section.

The maximum concentric gap, 2.35 mm and the minimum concentric gap, 0.35 mm are achieved by the inner PM ring of OD 6 mm and 10 mm respectively. When the assembly of 6 mm inner PM ring and 16 mm outer PM ring of length 1 mm is subjected to an axial displacement from the centered position to 1 mm with an increment of 0.2 mm in axial direction, the axial stiffness decreases by 7% with each increment, both numerically and experimentally. There is an approximate reduction of 5% and 3% in the axial stiffness for the lengths 2 mm and 3 mm of the PM rings (6 mm inner PM ring – 16 mm outer PM ring) respectively with 0.2 mm increment in the axial direction. The 10 mm inner PM ring – 16 mm outer PM ring assembly of length 1 mm when subjected to an axial displacement from the centered position to 1 mm with an increment of 0.2 mm in axial direction displays a 20% reduction in the axial stiffness with each increment, whereas there is a decrease of around 10% and 9% for the lengths 2 mm and 3 mm of this assembly, respectively. These results are plotted in figure (3-7).

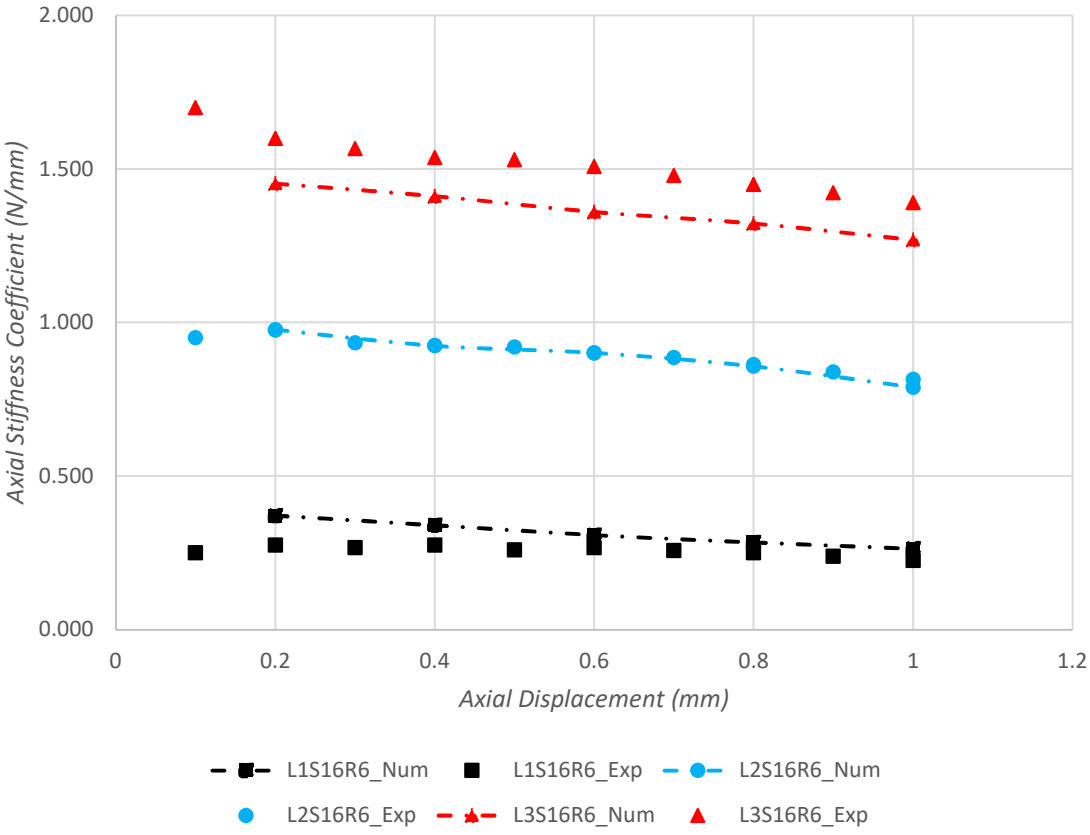

Figure 3-7 Change in Axial Stiffness for varying length with axial displacement for S16R6

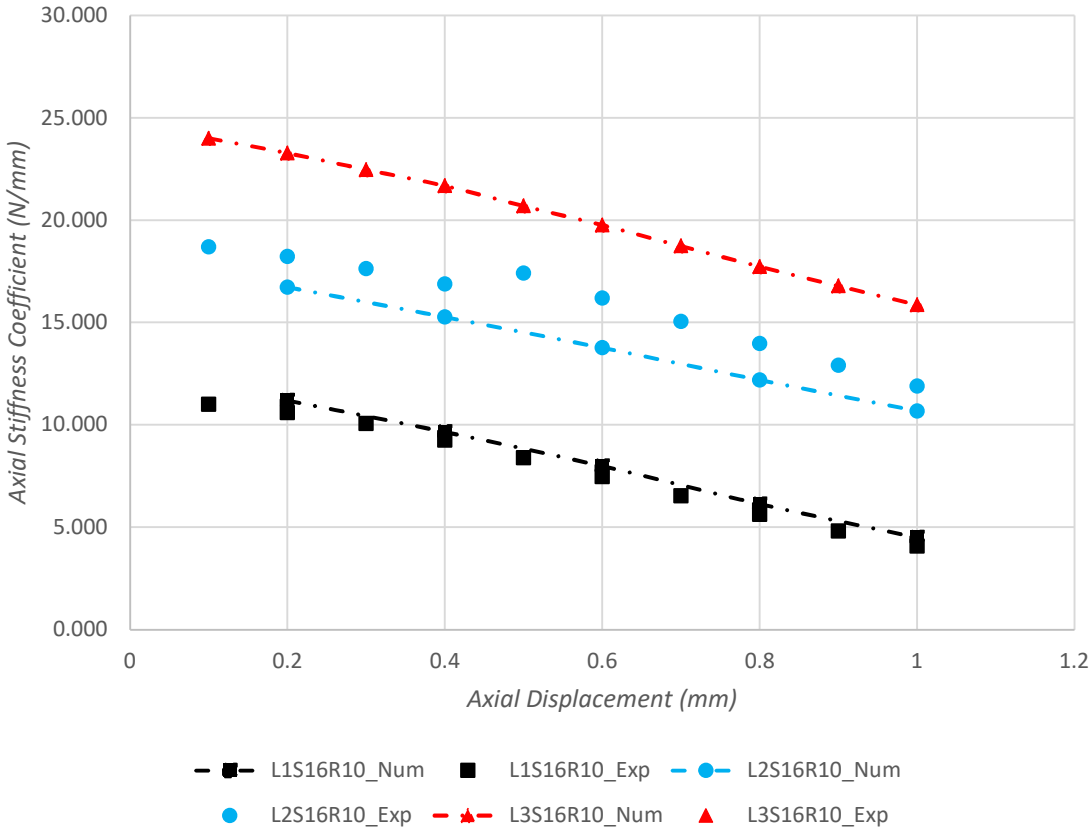

Figure 3-8 Change in Axial Stiffness with varying length with axial displacement for S16R10

When the 16 mm outer PM ring – 6 mm inner PM ring assembly is radially displaced from 0 mm (centered position) to 1 mm with 0.1 mm increment in radial direction, the radial stiffness for the length 1 mm and 2 mm increases by 2–3% for both with each increment. There is almost negligible increase in the radial stiffness for the 3 mm length for the discussed assembly with 0.1 mm increment in the radial direction. The 10 mm inner PM ring–16 mm outer PM ring assembly of length 1 mm when subjected to a radial displacement from the centered position to 1 mm with an increment of 0.1 mm in radial direction records a 4% increment in the radial stiffness with each increment, whereas there is an increase of around 2% for the 2 mm length and 3 mm length portrays negligible

increase in the radial stiffness of this assembly. These results are showed effectively by figures (3-9) and (3-10).

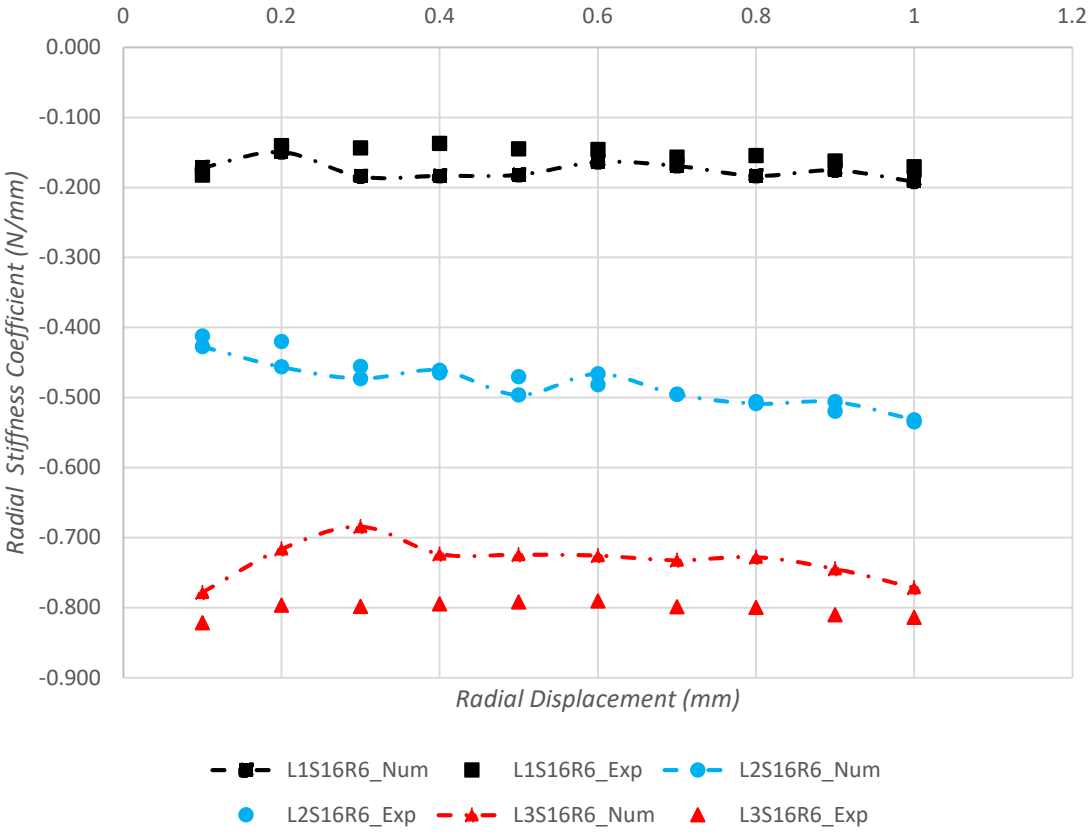

Figure 3-9 Change in Radial Stiffness for varying length with radial displacement for S16R6

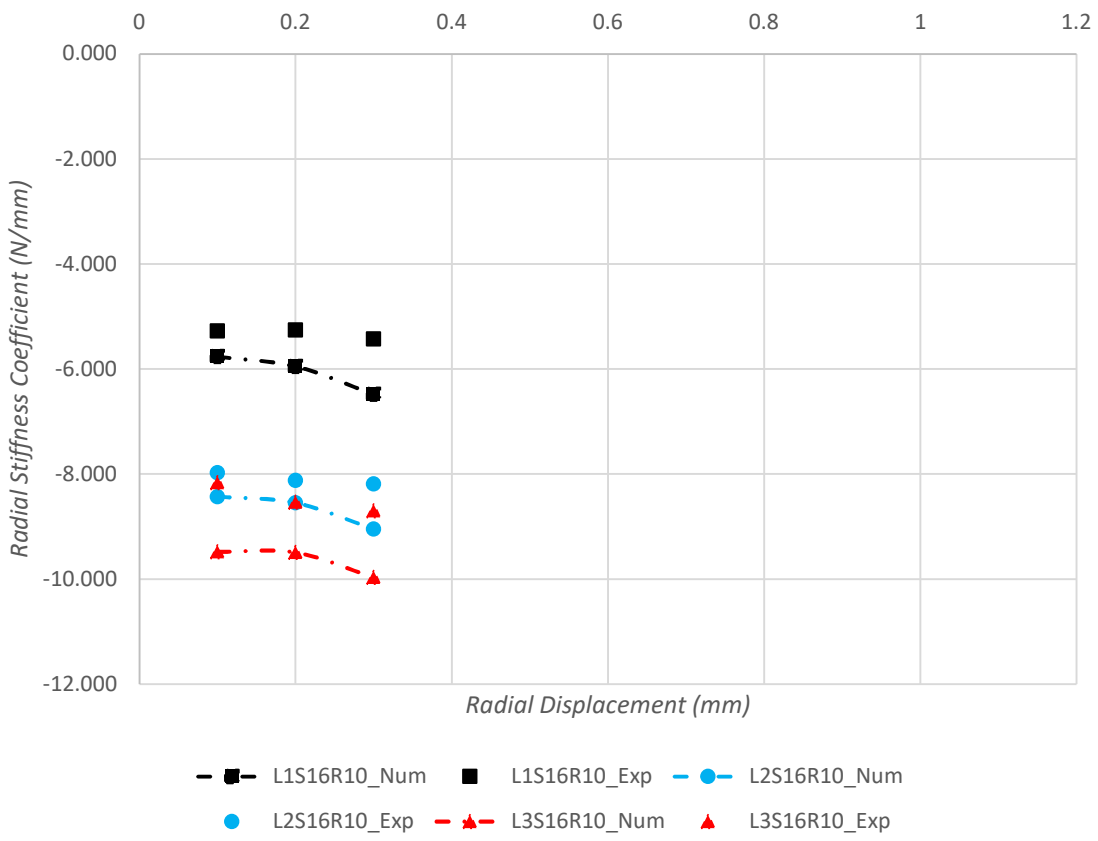

Figure 3-10 Change in Radial Stiffness for varying length with radial displacement for S16R10

Varying the length from 1 mm to 3 mm increases the axial stiffness and the radial stiffness by 5% approximately using both numerical and experimental methods.

3.1.2.3 Effect of change in OD of the outer PM ring

Three dimensions have been considered for the OD of the outer PM ring of the passive maglev system, namely, 16 mm, 18 mm, and 20 mm. The effect of the OD of the outer PM ring for the maximum and the minimum concentric gap of the PM rings assembly has been discussed in this section.

The maximum concentric gap, 2.35 mm and the minimum concentric gap, 0.35 mm are achieved by the inner PM ring of OD 6 mm and 10 mm respectively. When the

assembly of 6 mm inner PM ring – 16 mm outer PM ring (length 1 mm) is axial displaced from the centered position to 1 mm with an increment of 0.2 mm in axial direction, the axial stiffness decreases by 7% with each increment, both numerically and experimentally. There is an approximate reduction of 3% and 4% in the axial stiffness for the OD 18 mm and 20 mm of the PM rings (length 1 mm) respectively with 0.2 mm increment in the axial direction. The 10 mm inner PM ring – 16 mm outer PM ring assembly of length 1 mm when subjected to an axial displacement from the centered position to 1 mm with an increment of 0.2 mm in axial direction displays a 20% reduction in the axial stiffness with each increment. A similar reduction in the axial stiffness is observed for the OD 18 mm and 20 mm of the outer PM ring with each increment in the axial direction for a 10 mm inner PM ring of length 1 mm.

When the 6 mm inner PM ring (length 1 mm) assembly is subjected to a radial displacement from 0 mm (centered position) to 1 mm with 0.1 mm increment in radial direction, the radial stiffness for the 16 mm, 18 mm and 20 mm OD outer PM ring increases by 2–3% with each increment. The 10 mm inner PM ring–16 mm outer PM ring assembly (length 1 mm) when subjected to a radial displacement from the centered position to 1 mm with an increment of 0.1 mm in radial direction records a 4% increment in the radial stiffness with each increment. An equal an increase of 4% in the radial stiffness is observed for the OD 18 mm and 20 mm of the outer PM ring with each increment in the radial direction for a 10 mm inner PM ring of length 1 mm. Changing the outer diameter of the stator PM ring from 16 mm to 20 mm increases the axial and radial forces by 1% approximately, which is negligible compared to the effect of other geometric changes.

3.1.3 Discussion

The experimental and numerical results for 27 geometries of the concentric PM rings show that with a small axial displacement, the repulsive axial forces increase, indicating axial instability. Under radial displacement, the radial force also becomes repulsive, indicating radial stability. Repulsive forces in the axial direction drive the rings further apart, while repulsive forces in the radial direction drives the inner PM ring back to its concentric position.

It can be interpreted that the 6 mm inner PM ring provides the maximum concentric gap but generates weaker magnetic forces with axial and radial displacement. The 8 mm inner PM ring and 10 mm inner PM ring provide a concentric gap of 1.35 mm and 0.35 mm respectively which are less compared to 2.35 mm gap achieved by using 6 mm inner PM ring. Whereas, the axial and radial stiffness of 8 mm and 10 mm inner PM ring is higher, and these dimensions would compensate the radial forces generated by the BLDC motor rotor eccentricity more efficiently than 6 mm inner PM ring.

3.1.4 Conclusion

In this study, 27 geometries of different OD of the inner PM ring, OD of the outer PM ring and the length of the PM rings for the concentric arrangement of the PM rings in the passive magnetic levitation system have been analyzed using the numerical and the experimental methods. The numerical methods involve the finite element model simulation using COMSOL 5.4 for the evaluation of the magnetic forced generated in the concentric PM ring assembly with respect to axial and radial displacements. The experimental study was carried out using a custom magnetic force test rig at Center for Technology Innovation, Texas Heart Institute (Houston, TX). The results from the numerical and the experimental

evaluation were assessed by calculating the axial stiffness coefficient and the radial stiffness coefficient. This study serves as a data base of 27 geometries of the PM rings assembly to provide information related to the concentric gap, the stiffness coefficient and its behavior with respect to displacement. This data base will help in selection of the PM rings in the passive magnetic levitation system in the BSSD to counteract the radial forces induced by the BLDC motor rotor eccentricity.

3.2 Brushless DC Motor

The blood shear stress device uses an electronically commutated (EC) 3-phase brushless direct current (BLDC) motor purchased from Maxon Precision Motors, Inc. (125 Dever Drive, Taunton, MA 02780, United States). The BLDC motor consists of a stationary iron stator with an inner layer of copper winding and a rotating rotor, comprised of an iron shaft encapsulated within permanent magnets, inside this layer.

The BLDC motor operation is based on simple force interaction between an electromagnet and a permanent magnet. The layer of copper winding located inside the stator consists of multiple coils. By applying direct current (DC) power to a coil, the coil will energize and become an electromagnet. In this condition, the opposite poles of the rotor and the stator are attracted to each other. As the rotor moves closer to the coil, next coil is energized causing the rotor to move towards this coil. This process is repeated, and the rotor continues to rotate.

As BLDC motor offers high power-to-weight ratio, high speed, electronic control, and low maintenance, it is used in magnetic levitation technologies in medical devices. Though at high rotational speeds, the rotor of the BLDC motor becomes radially unstable, and tends to move radially. In order to achieve magnetic levitation in BSSD, the passive maglev system is used to radially stabilize the BLDC motor rotor. Section 3.1 analyzes different PM ring geometries for the BLDC motor rotor stabilization. Section 3.2 evaluates 10 geometries of varying the BLDC motor rotor sizes, listed in table (3-3), for studying the generated back electromotive force and the torque constant. Also, these 10 geometries are studied for the assessment of the induced magnetic forces within the BLDC motor due to radial eccentricity of the rotor with 0.1 mm increment in the radial direction.

Table 3-3 List of considered BLDC motor geometries

Geometry	Stator Inner Diameter (mm)	Winding Inner Diameter (mm)	Rotor Outer Diameter (mm)
1.	13.35	10.7	10.4
2.	13.35	10.7	10
3.	13.35	10.7	9.5
4.	13.35	10.7	9
5.	13.35	10.7	8.5
6.	13.35	10.7	8
7.	13.35	10.7	7.5
8.	13.35	10.7	7
9.	13.35	10.7	6.5
10.	13.35	10.7	6

3.2.1 Methods

This section explores the numerical and experimental methods to study the dynamic testing and the static testing of the BLDC motor. The dynamic testing evaluates the generated back electromotive force and the torque constant with change in the BLDC motor rotor OD whereas the static testing assesses 10 geometries for the behavior of the induced magnetic forces within the BLDC motor due to radial eccentricity of the rotor with 0.1 mm increment in the radial direction. Section 3.2.1.1 discusses the finite element method analysis of a 2-dimensional geometry of the BLDC motor using numerical simulation software COMSOL 5.4 for both dynamic and static testing. Section 3.2.1.2 elaborates the

experimental methods to analyze the generated radial forces in 10 BLDC motor geometries of varying the motor rotor diameter with a 0.1 mm radial displacement increment using a custom-made test rig.

3.2.1.1 Numerical Methods

The BLDC motor is evaluated using FEM in numerical simulation software COMSOL 5.4 to effectively design the magnetic levitation technology and stabilize the rotor of the BLDC motor radially in the BSSD. Based on the measurements made after disassembling the ECX 22 brushless DC (BLDC) motor, a 2-dimensional geometry was built in COMSOL 5.4. The BLDC 2D model consists of a stationary stator with an inner layer of copper winding and a rotating rotor inside this layer. As observed while disassembling the motor, the winding layer consists of coils and a multitude of turns in each coil. These coils are found to be in an overlapping and slant arrangement in order to reduce the effect of torque ripple. In order to replicate this, the winding layer of the 2D model has 30 coils, each of 0.33 mm diameter.

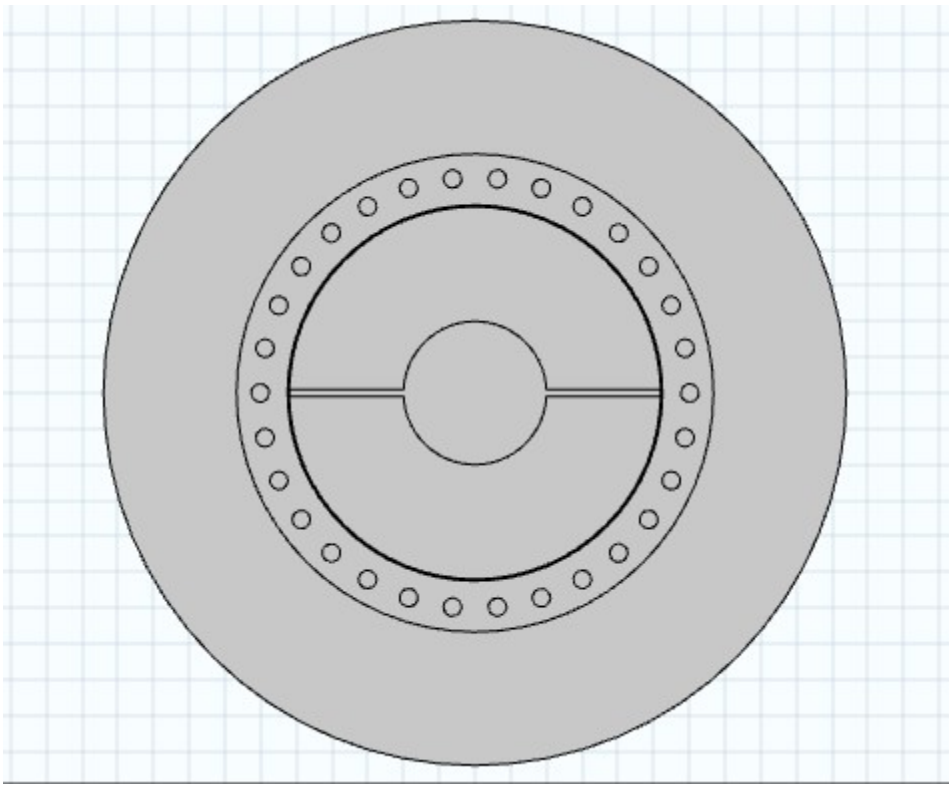

Figure 3-11 A 2-D geometry of BLDC stock motor in COMSOL 5.4

The outer diameter (OD) and the inner diameter (ID) of the stator are 20.8 mm and 13.35 mm respectively. The winding layer inside the stator is 1.325 mm thick with an ID of 10.7 mm. It consists of 30 coils of 0.5 mm diameter. The rotor comprises a 4 mm diameter shaft and two semi-circular 10.4 mm diameter permanent magnets encapsulating the shaft. This rotor assembly is set as rotating domain at 20,000 rpm. The stator and the shaft are assigned soft iron as the material from the COMSOL material data base, whereas the permanent magnets are treated as air.

A user defined fine mesh is created using tetrahedrons with maximum and minimum element size of 0.1 mm and 0.001 mm respectively. The mesh is calibrated for general physics with maximum element growth rate of 1.1.

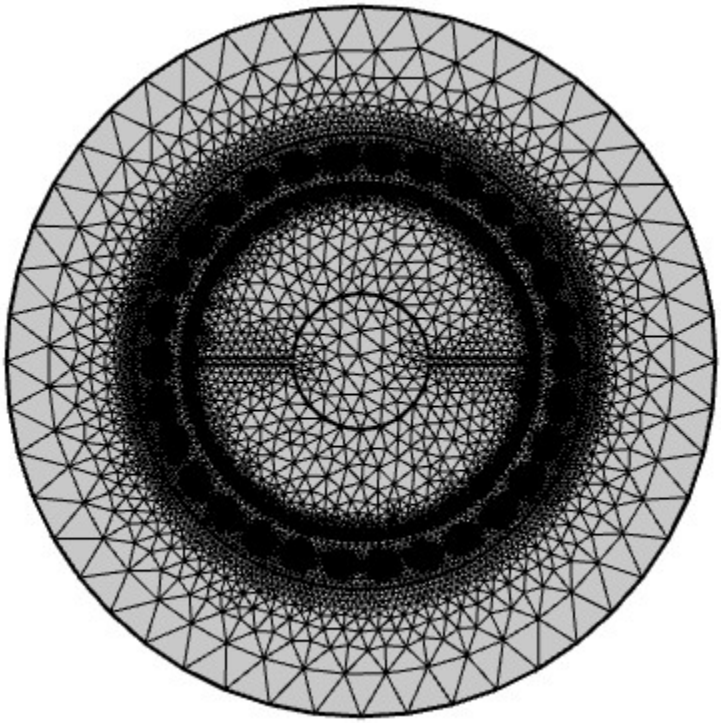

Figure 3-12 A user defined mesh for the BLDC stock motor in COMSOL 5.4

A *Rotating Machinery, Magnetic* interface is employed for this 2-dimensional geometry of BLDC motor. This interface solves the Maxwell's equations formulated using the magnetic vector potential, A and magnetic scalar potential, V_m as the dependent variables with an initial value of 0 Wb/m and 0 A, respectively [48].

Ampere's Law is applied to permanent magnets, namely, PM inwards and PM outwards, where the magnetic field, B is calculated by

$$B = \mu_0 \mu_r H + B_r, \tag{3-7}$$

where $\mu_0$is the permeability of vacuum, 1.257e-06 H/m, μ_r is the relative permeability obtained from the material and B_r is the remanent flux density, -1.0 T (PM inwards) and 1.0 T (PM outwards).

Ampere's Law is applied to the BLDC stator and the shaft where the magnetic field, B is calculated using H-B curve as the constitution relation.

$$H = f(|B|)\frac{B}{|B|}, \tag{3-8}$$

where H is the Magnetic Field Intensity, A/m and B is the magnetic field density, T.

Since this BLDC motor uses 3-phase power input to the coils, the 30 coils are divided in 3 groups with 10 coils in each group. Each of these groups functions as a phase in the model setup. Each phase is assigned as a homogenized multiturn coil with a coil current of 0 A. The homogenized multiturn coil consists of 0.33 mm diameter with 9 turns. A reverse current direction is applied to half of the coils in each phase. The magnetic field, B is calculated by

$$B = \mu_0 \mu_r H, \tag{3-9}$$

where $\mu_0$is the permeability of vacuum, 1.257e-06 H/m, μ_r is the relative permeability.

The magnetic forces generated within the BLDC motor due the rotor eccentricity is governed by the equation (3-10)

$$F = \oint nT \, dS. \tag{3-10}$$

The back EMF, V and the coil resistance, Ω for each multiturn coil is obtained as an output of the simulation. This back EMF is used to calculate the speed constant, $K_s$and the torque constant, K_t for 10 geometries of varying BLDC motor rotor size using the following relations

$$K_s = \frac{20000}{Back\ EMF}\ min^{-1}V^{-1}\text{ , and} \tag{3-11}$$

$$K_T = \frac{6*10^4}{2\pi}\frac{1}{K_s}\ mNmA^{-1}. \quad (3\text{-}12)$$

The BLDC motor rotor of each geometry is subjected to radial displacement with 0.1 mm increment in the radial direction depending on the available concentric gap using a parametric sweep. The induced radial magnetic forces are obtained as an output from the FEM analysis and the radial stiffness coefficient for the BLDC motor is calculated using the following equation.

$$k_{rotor\_r} = \frac{F_{rotor\_r}}{\Delta r}\ when\ \Delta z = 0, \quad (3\text{-}13)$$

where Δz is the axial displacement, mm and Δr is the radial displacement, mm. F_{rotor_r} is the radial magnetic force generated due to radial displacement of the rotor, N and k_{rotor_r} is the radial stiffness coefficient of the BLDC motor, N/mm.

3.2.1.2 Experimental Methods

The experimental setup for the assessment of the radial forces generated within the BLDC motor due to the displacement in the radial direction uses the aluminum magnetic force test rig described in Section 3.1.1.2 with exchangeable parts.

Figure (3-13) shows the assembly of the custom test rig designed by Dr. P. Alex Smith, Research Engineer III using Solidworks at Center for Technology Innovation, Texas Heart Institute (Houston, TX).

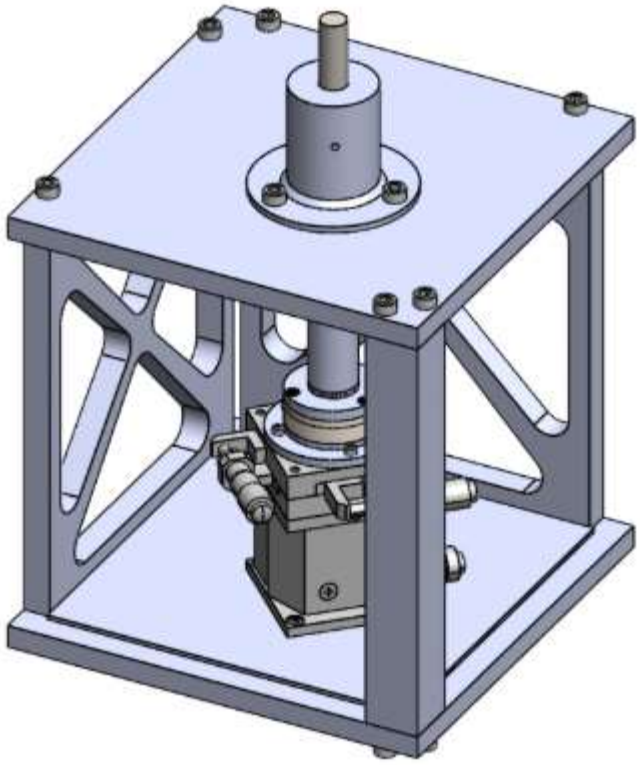

Figure 3-13 An assembly of manufactured Magnetic Force Test Rig for static testing of BLDC motor geometries

In the magnetic force test rig, the inner PM ring holder is replaced with collet holder mount to align the BLDC motor rotor concentrically with the stator. The outer PM ring holder and the PM ring retention are replaced by motor stator holder.

These components were manufactured at by Juan Fernandez, Lead Machinist at Houston Methodist Research Institute (Houston, TX). The magnetic force test rig was assembled at Center for Technology Innovation, Texas Heart Institute (Houston, TX). The radial displacement in the x direction is achieved with a highly precision stainless-steel x-y-z stage (XYSSG60 and ZLPGS60, MiSUMi Group, Inc., Tokyo, Japan) moved by a micrometer head. The BLDC motor rotor, held in place by motor stator holder, is mounted on a force transducer (Nano43, ATI Industrial Automation, Apex, NC, USA). The force

transducer is mounted on the x-y-z stage. The collet holder mount is then set up on the top plate with BLDC motor rotor held in position. The output given by the force transducer using a Simulink code as a result of the displacement in the x direction are acquired using by a dSpace MicroLabBox (DS1202, dSPACE Inc., Paderborn, Germany).

The first step towards the magnetic force testing on the test rig involves mounting the BLDC motor stator on the force transducer using motor stator holder. This is followed by taring of the forces generated in the x, y and z direction due to weight of the motor stator. The BLDC motor rotor is then placed concentrically with the stator collet holder mount fixed on the top plate of the test rig. The center alignment of the BLDC motor rotor with respect to the BLDC motor stator is achieved by adjusting the micrometer head until the forces in the x, y, z direction is null.

The BLDC motor rotor is then subjected to radial displacement with the help of micrometer gauge from the centered position with 0.1 mm increment in in x direction with respect to available concentric gap. The generated radial forces are recorded, and the BLDC motor rotor is brought to the initial position.

The above-mentioned testing process is performed for each of the 10 geometries of varying BLDC motor rotor sizes. The results are used to calculate the radial stiffness to efficiently design the magnetic levitation technology for the BSSD.

3.2.2 Results

The numerical evaluation for the dynamic and the static testing of the 10 geometries of different BLDC motor rotor sizes has been performed. Due to occurrence of unforeseen/ unexpected issues, the experimental evaluation for the static testing of the BLDC motor

could not be achieved. This section describes the FEM analysis results using numerical methods for (1) Dynamic Testing and (2) Static Testing. It also mentions the issues faced during the static testing using experimental evaluation methods.

3.2.2.1 Numerical Methods: Dynamic Testing Results

A robust FEM BLDC model is achieved with an error of less than 1% on the simulation software COMSOL 5.4 by using the BLDC stock motor with the rotor diameter of 10.4 mm to get a back EMF of 18.5 V by varying the coil wire diameter, number of coils and number of turns. These results are then validated using the motor specification sheet, which gives us a back EMF of 18.34 V from the speed constant of 1090 $min^{-1}V^{-1}$ using equation (3-11).

The dynamic testing evaluates 10 BLDC motor geometries including rotor sizes 6 mm to 10 mm with 0.5 mm increment with each geometry and BLDC stock motor. When the centered BLDC motor stator-rotor arrangement is subjected to change of the rotor sizes, the back EMF generated in each phase increases linearly from 5.46 V for a 6 mm rotor size to 18.34 V for a 10.4 mm rotor size with an approximate increase of 116% with each geometry. The results are plotted in the figure (3-14).

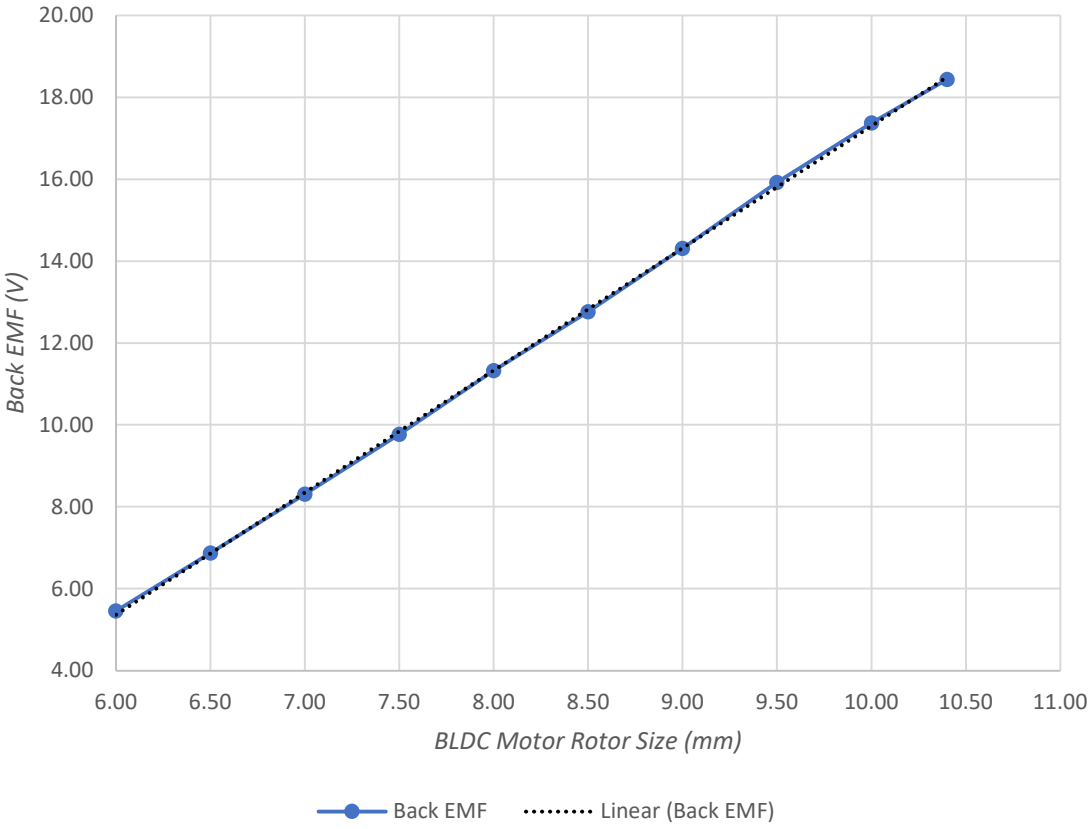

Figure 3-14 Change in Back EMF (V) with BLDC Motor Rotor Size (mm)

An approximate change between 85% - 90% is observed in the speed constant, K_s with the change in the BLDC motor rotor size from 6 mm to 10.4 mm. The values depreciate from 3665.11 $min^{-1}V^{-1}$ to 1084.91 $min^{-1}V^{-1}$. These results can be observed in figure (3-15).

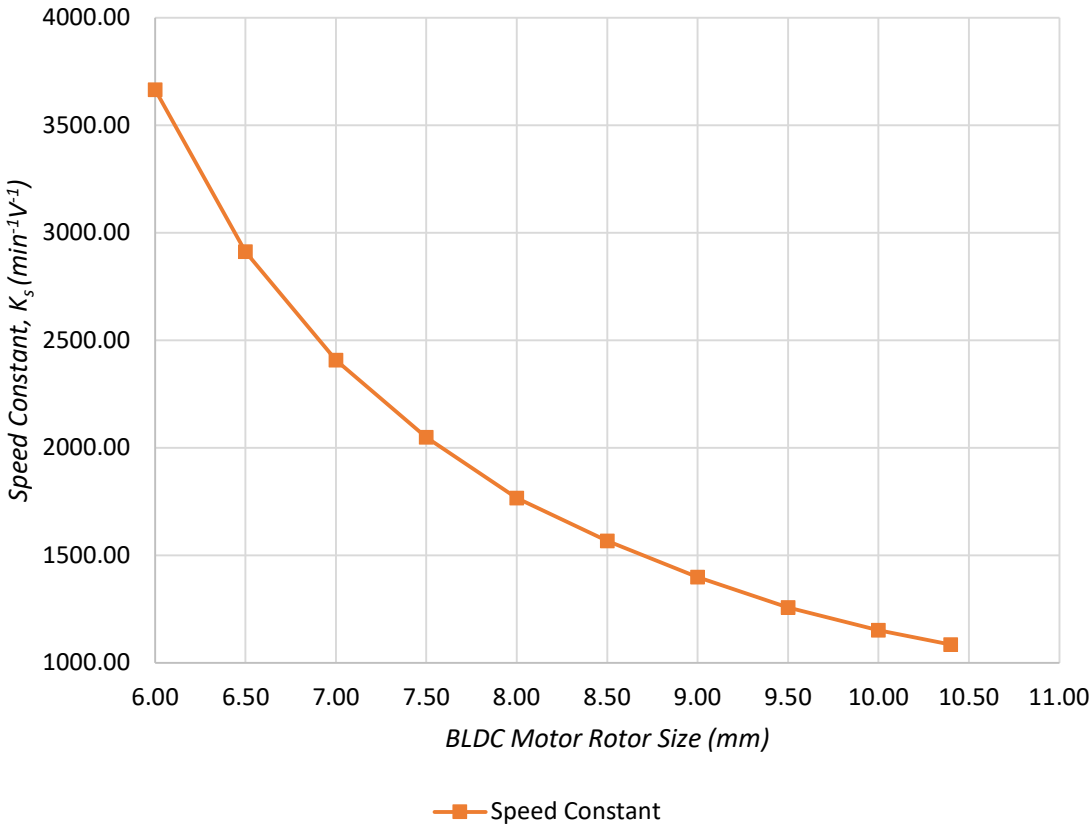

Figure 3-15 Change in Speed Constant, Ks (min-1V-1) with BLDC Motor Rotor Size(mm)

The torque constant, K_t undergoes a similar linear change like the back EMF when the BLDC motor rotor size is varied from 6 mm to 10.4 mm (with 0.5 mm increment from 6 mm to 10 mm). The torque constant, K_t is obtained by using the equation (3-12). The results are presented in the plot in figure (3-16).

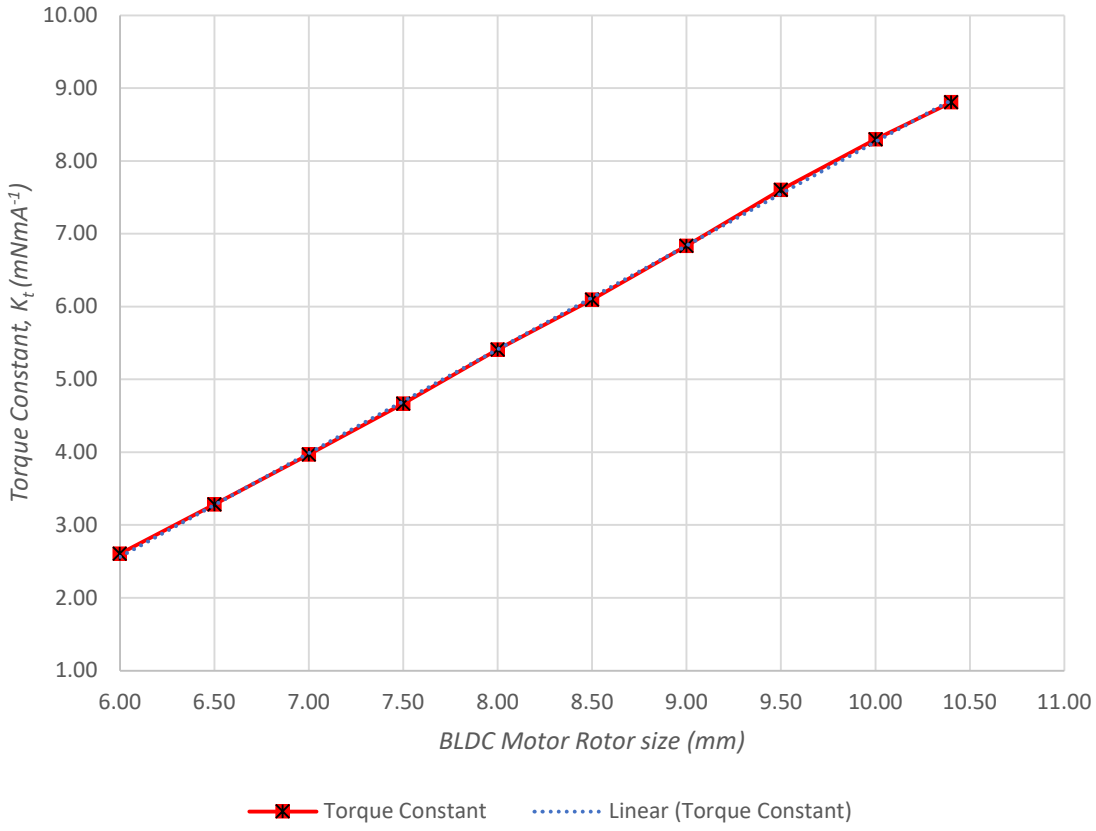

Figure 3-16 Change in Torque Constant, Kt (mNmA-1) with BLDC Motor Rotor size (mm)

3.2.2.2 Numerical Results: Static Testing

The static testing is performed by giving the BLDC motor rotor for each of 10 geometries mentioned in table (3-3) a 0.1 mm radial displacement increment with the permissible concentric gap to analyze the radial stiffness of the BLDC motor geometries. The BLDC stock motor (10.4 mm) gives a concentric gap of 0.15 mm, hence the results can be neglected. As the BLDC motor rotor size varies from 6 mm to 10 mm, the concentric gap decreases from 2.35 mm to 0.35 mm. The maximum and the minimum concentric gap is given by using the BLDC motor rotor of size 6 mm and 10 mm respectively. The table (3-4) states all the motor rotor sizes along with their gap sizes.

Table 3-4 List of BLDC geometries with their concentric gap sizes

Geometry	Stator Inner Diameter (mm)	Winding Inner Diameter (mm)	Rotor Outer Diameter (mm)	Concentric Gap Size (mm)
1.	13.35	10.7	6	2.35
2.	13.35	10.7	6.5	2.10
3.	13.35	10.7	7	1.85
4.	13.35	10.7	7.5	1.60
5.	13.35	10.7	8	1.35
6.	13.35	10.7	8.5	1.10
7.	13.35	10.7	9	0.85
8.	13.35	10.7	9.5	0.60
9.	13.35	10.7	10	0.35
10.	13.35	10.7	10.4	0.15

For the 6 mm BLDC motor rotor, the radial stiffness coefficient changes from 6.56 N/mm to 3.10 N/mm when a radial displacement from 0 mm to 2.30 mm is applied with 0.1 increment in the radial direction. For a 10 mm BLDC motor rotor, the radial stiffness coefficient decreases from 35.12 N/mm to 33.75 N/mm with radial displacement in the available gap size. The behavior of the radial stiffness coefficient for 9 out of 10 geometries can be studied from figure (3-17). An increase of 28.56 N/mm to 30.55 N/mm is recorded in the k_{rotor_r} when the BLDC motor rotor is changed from 6 mm to 10 mm.

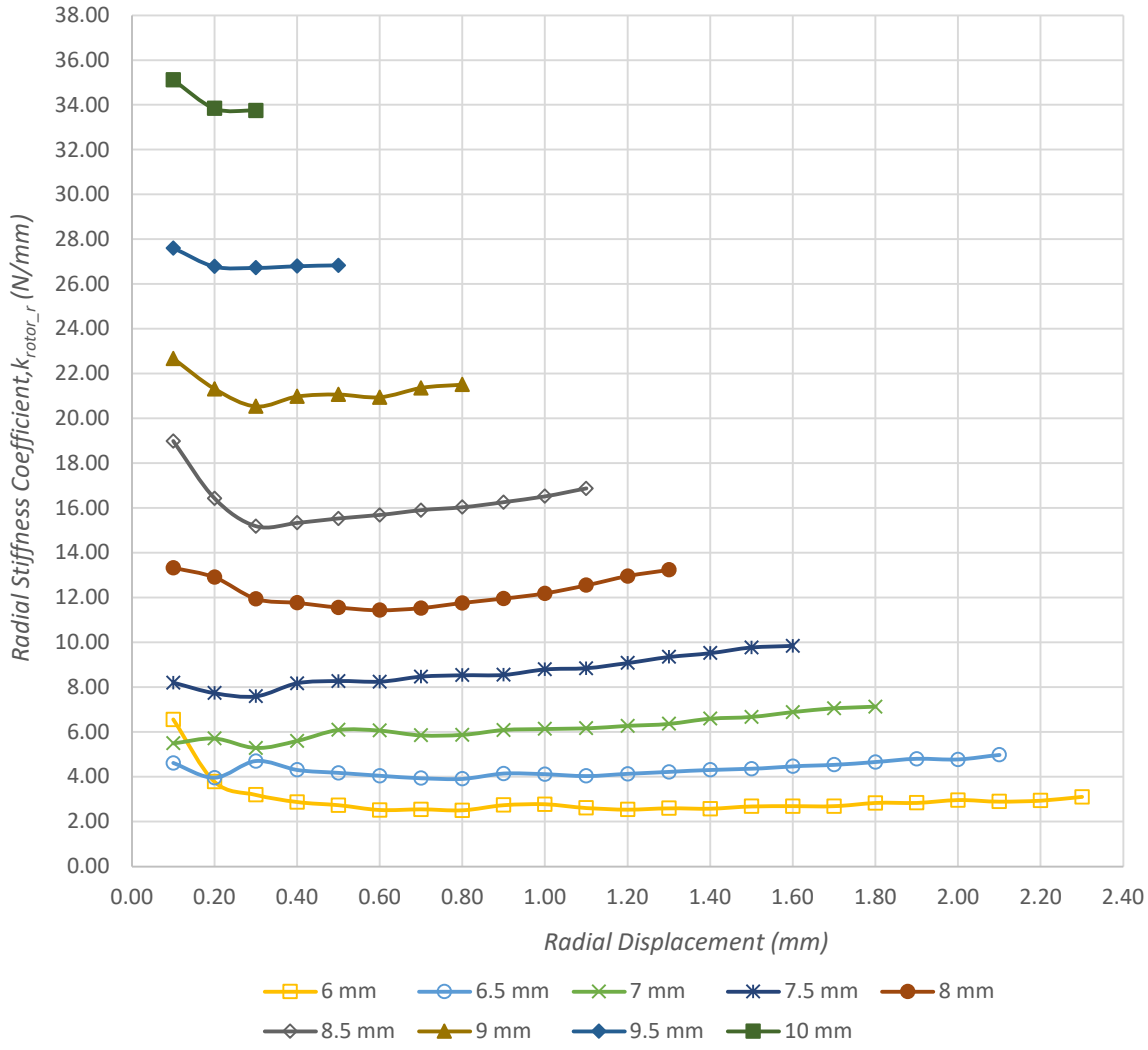

Figure 3-17 Change in Radial Stiffness Coefficient, k_{rotor_r} (N/mm) with Radial Displacement (mm)

3.2.2.3 Challenges associated with Experimental Methods

The experimental evaluation for the static testing of the BLDC motor rotor could not be accomplished because of experiencing unexpected challenges with achieving radial stability, center alignment of the BLDC motor rotor. Due to high magnetic forces within the BLDC motor, the motor rotor was attracted towards the inner surface of the winding during the experiment setup. These strong magnetic forces made achieving the radial

stability completely impossible. Inability to achieve a centered concentric alignment due to high magnetic forces and the test rig design played a significant role towards the issue. When an almost radially stable BLDC motor rotor size 6 mm was mounted on the test rig and subjected to radial displacement, the axial forces varied by large values. We are still investigating the cause for such behavior.

3.2.3 Discussion

The numerical results for the dynamic testing of 10 geometries of the BLDC motor rotor show that with an increase in the motor rotor size, the back EMF and the torque constant increase in a similar pattern, whereas there is a significant reduction in the speed constant. The back EMF regulates the flow of winding current, as the back EMF increases the winding current decreases. The torque constant calculations will facilitate the selection of an appropriate BLDC motor size for the BSSD considering the design limitations.

Under radial displacement of the BLDC motor rotor, the radial force increases indicating radial instability. These magnetic forces in the radial direction pushes the BLDC motor rotor towards the winding. It can be interpreted that the 6 mm BLDC motor rotor provides the maximum concentric gap but generates weaker magnetic forces radial displacement. As the gap size reduces, the radial forces grow with radial displacement. The radial stiffness of larger BLDC motor rotor sizes suggests that it would need strong radial forces generated by the PM rings in order to achieve magnetic levitation efficiently.

3.2.4 Conclusion

In this study, 10 geometries of different BLDC motor rotor sizes for achieving the magnetic levitation of the BLDC motor rotor in the BSSD have been analyzed using the numerical dynamic testing method and the numerical static testing method. The numerical

methods involve the finite element model simulation using COMSOL 5.4 for the 2-dimensional BLDC motor geometry. The results from the dynamic testing were assessed by calculating the speed constants and the torque constants using the generated back EMF. The static testing involved the calculation radial stiffness coefficient when the BLDC motor geometries are subjected to radial displacement. This study serves as a data base of 10 geometries of the varying BLDC motor rotor sizes to enable the selection of the suitable dimension for the BLDC motor to incorporate magnetic levitation of the motor rotor successfully in the BSSD considering the design and application limitations. The data will also server in selection of the magnetic bearings for the passive magnetic levitation system.

Chapter 4 CFD Modeling for BSSD

Computational Fluid Dynamics (CFD) is a rapidly developing approach towards solving the fluid flow equations using numerical methods for the fluid flow analysis and prediction. CFD modeling of the fluid helps in the prototype testing and failure analysis of the engineering design, thereby, saving cost and time. Major application areas for CFD include aerodynamics, weather simulations, industrial design and failure analysis, biomedical engineering, engines, turbines, etc.

In cardiovascular diseases and the development of the devices like VADs, CFD has proven to be an important tool for predicting hemolysis and platelet activation due to the device interaction with blood in the physiological environment [Fraser 2011]. It is very useful in testing different designs for a wide range of operating conditions, thereby saving cost for prototype testing. In-silico (computational) modeling prior to animal implants might lead to design improvement and modifications which could prevent unnecessary animal sacrifice.

CFD analysis for assessing the blood flow and the hemolysis caused in LVADs as well as TAH have been performed [49-59]. The flow induced hemolysis is dominated by two factors shear stress and exposure time. M. Giersiepen [57] established a power law model which is a quantitative correlation between hemolysis and flow dependent factors. The power law is

$$D = A\tau^{\alpha}t^{\beta}, \tag{4-1}$$

here, D is the rate of generation of plasma-free hemoglobin, τ is the shear stress exposed to the red blood cells, and t is the exposure time. The model constants A, α and β were obtained from the experimental data.

New empirical constants were obtained for the power law model using Couette-type shearing devices with rotating inner cylinder and concentric stationary outer housing given by

$$IH_{flow} = 1.228 \times 10^{-5} \times \tau^{1.9918} \times t^{0.6606}, \quad (4\text{-}2)$$

here, IH_{flow} refers to the flow induced index of hemolysis by the device, which is a measure of blood damage caused. The measured hemolysis using these constants was within the same order of magnitude as Paul et al.'s study but much less than Giersiepen et al.'s study [57]. This confirmed the overestimation of hemolysis in Giersiepen et al.'s study.

This chapter describes the CFD modeling of blood flow through the annular gap between the rotating rotor and the stationary stator of the BSSD. The hemolysis index calculation is accomplished using the relation in (4-2). Modeling fluid flow using CFD involves identifying the type of fluid, the type of fluid flow and then determining the fluid properties.

Fluid can be categorized based on the shear stress and the velocity gradient relationship:

1. Ideal fluid: It is incompressible and has no viscosity. This type of fluid does not physically exist.
2. Real fluid: It has viscosity.

3. Newtonian fluid: A real fluid whose shear stress is directly proportional to the velocity gradient, is called Newtonian fluid.
4. Non-Newtonian fluid: A real fluid, in which shear stress is not directly proportional to the velocity gradient, is known as non-Newtonian fluid. At larger scale, blood can be modeled as Newtonian fluid.
5. Ideal plastic fluid: A fluid, in which shear stress is more than the yield value and shear stress is proportional to the rate of velocity gradient, is known as ideal plastic fluid.

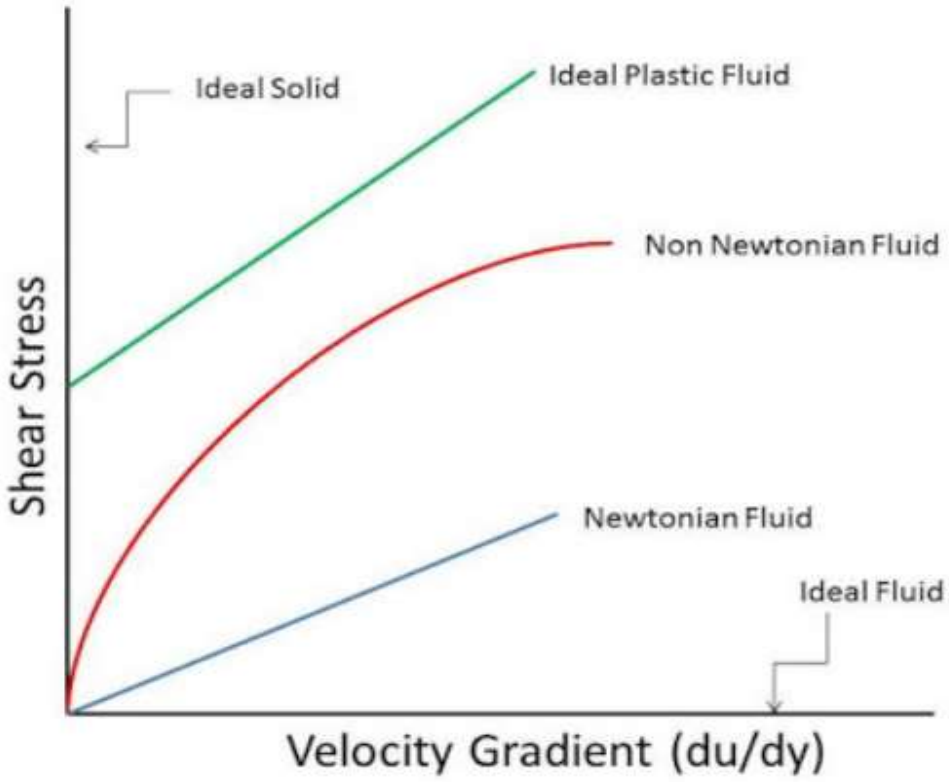

Figure 4-1 Types of fluids

The types of fluid flow are listed as follows:

1. Steady and Unsteady flow: A steady flow can be defined as a flow in which the flow characteristics like velocity, pressure, density, etc at a point do not change with respect to time. In an unsteady flow, the fluid flow characteristics at a point change with time.
2. Uniform and Non-uniform flow: A uniform flow can be defined as a flow in which the velocity at any given time is constant in space. In a non-uniform flow, the velocity at any given time changes in space.
3. Laminar and Turbulent fluid flow: In Laminar fluid flow, the fluid particles move along well-defined smooth streamlines, these streamlines are straight and parallel. The fluid particles move in an irregular pattern forming eddies in a turbulent fluid flow.
4. Compressible and Incompressible fluid flow: A compressible fluid flow can be defined as a flow in which the Mach number >0.3. In an incompressible flow, the Mach number is less than 0.3.
5. Rotational and Irrotational flow: A fluid flow in which the particles rotate about their own axis while flowing along a streamline is called a rotational flow. In an irrotational flow, the fluid flow particles do not rotate about their on axis.

Section 4.1 describes the fluid flow in the annular gap between the rotor and the stator in the BSSD. This helps in CFD modeling needed to predict the maximum blood damage in an operational BSSD.

4.1 Flow in an Annulus

In an operational BSSD, the pressure driven blood passes through the narrow annular gap between the rotating BLDC motor rotor and the stationary BLDC motor stator in the axial direction. This resulting flow can be treated as the superposition of circular

Couette flow and axial Poiseuille flow and can be termed Taylor-Couette-Poiseuille flow or spiral Poiseuille flow [70].

The Poiseuille law for the laminar axial flow in a circular cross-section pipe is given by

$$Q = \frac{\pi * R^4 * \Delta p}{8 * \mu * l}, \tag{4-3}$$

where Q is the flow rate; R is the radius of the pipe, Δp is the pressure difference between the inlet and the outlet, μ is the dynamic viscosity of the fluid and l is the length of the pipe.

It is important to examine some non-dimensional parameters in order achieve Couette flow as well as effectively simulate the flow through BSSD [72-79]

Axial Reynolds number, $Re_{axial} = \frac{\rho * V * D}{\mu}$, (4-4)

Circumferential Reynolds number, $Re_c = \frac{\rho * \omega * R_i * h}{\mu}$, and (4-5)

Taylor number, $Ta = {Re_c}^2 \frac{h}{R_i}$, (4-6)

where ρ is the density of the fluid, V is the axial velocity, ω is the angular velocity of the rotating cylinder/ rotor, h is the annular gap size.

4.2 Methods

This section describes the CFD modeling methods used to study the maximum shear stress caused by the rotating BLDC rotor of a functional BSSD. In order to build a reliable CFD model for the BSSD, two separate cases for Poiseuille flow and Couette flow have been solved using ANSYS Fluent 19.0. The results for these flows have been validated with values from the analytical equations mentioned in section 4.1. A CFD model

is solved for 3 different flow rate values of the axial flow in 2 different annular gap sizes using ANSYS Fluent 19.0. The details are given in the following table:

Table 4-1 List of BSSD geometries for CFD analysis

Geometry	Flow rate, Q (mL/min)	ID of the Winding (mm)	OD of the Rotor (mm)	Annular Gap Size (mm)
1	100	10.7	6	1.35
2	100	10.7	8	2.35
3	200	10.7	6	1.35
4	200	10.7	8	2.35
5	300	10.7	6	1.35
6	300	10.7	8	2.35

Section 4.2.1 explains the geometry and the mesh created for Poiseuille flow, Couette flow and flow through the annular gap in BSSD. Whereas, section 4.2.2 discusses the model setup for the aforementioned cases.

4.2.1 Geometry and Mesh

A 3-dimensional pipe with circular cross-section of diameter 1 m and length 10 m is created in Fluent R19.0 for the Poiseuille flow simulation. Figure (4-2) shows the geometry for the Poiseuille flow.

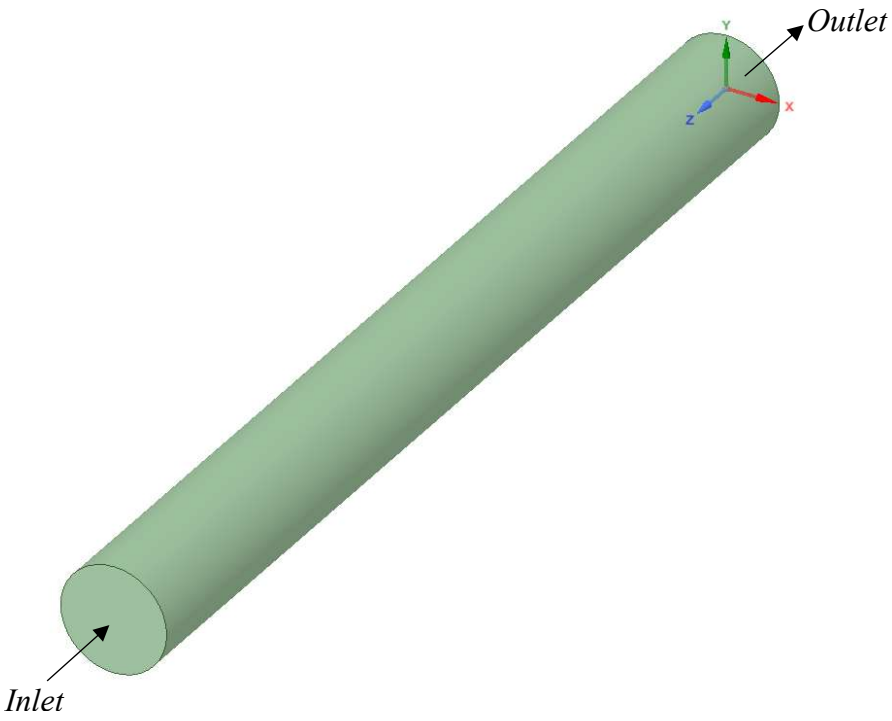

Figure 4-2 3D geometry for Poiseuille flow simulation

The sweep mesh with 200 divisions is generated for the geometry in figure (4-2) using the inlet and the outlet of the pipe as the source and the target respectively. The maximum face size is set to 0.025 m for a fine mesh with 458200 number of elements. Figure (4-3) shows the zoomed-in image of the generated mesh with an inflation layer of 100 for effective modelling of the boundary layers in the pipe.

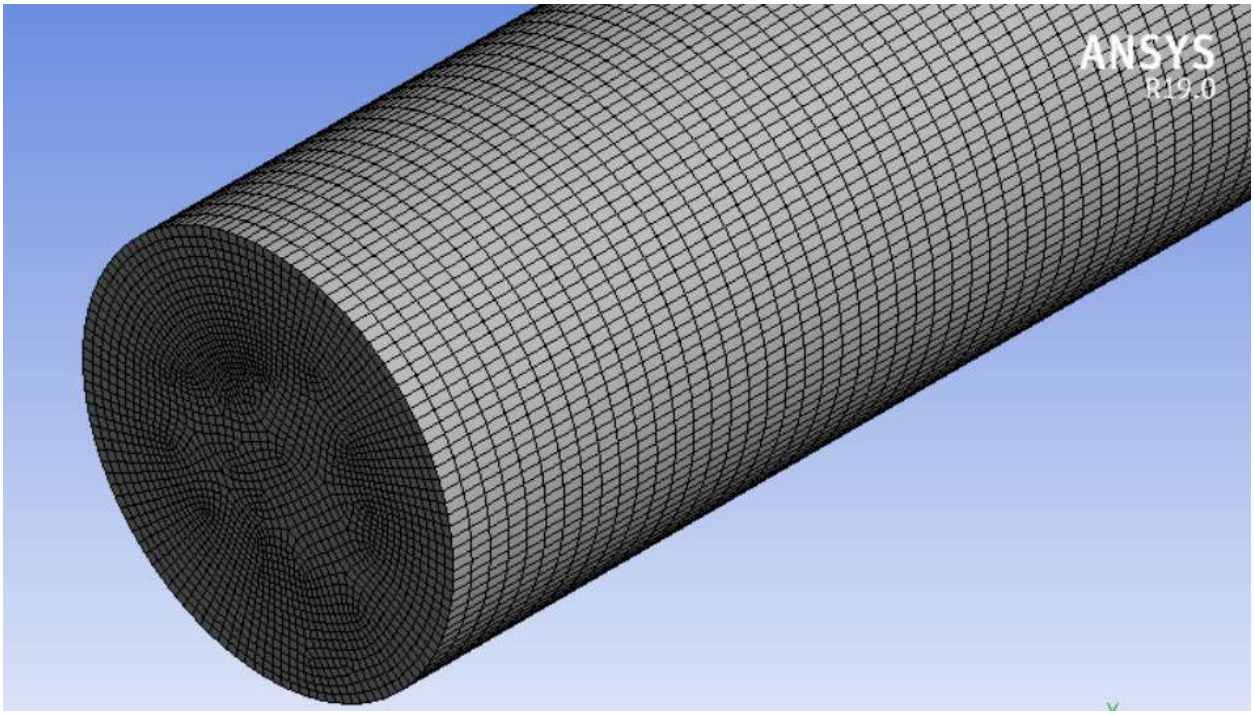

Figure 4-3 Mesh generated for the Poiseuille flow simulation

For the Couette flow simulation, a 3-dimensional 30^{o} sector representing concentric cylinders with annular gap size of 0.25 m and length 5 m is created in Fluent R19.0. Only a small angular segment of the entire annulus is modeled in order to save computational time. The figure (4-4) shows the geometry for Couette flow. There are periodic boundary conditions in the angular (θ) direction.

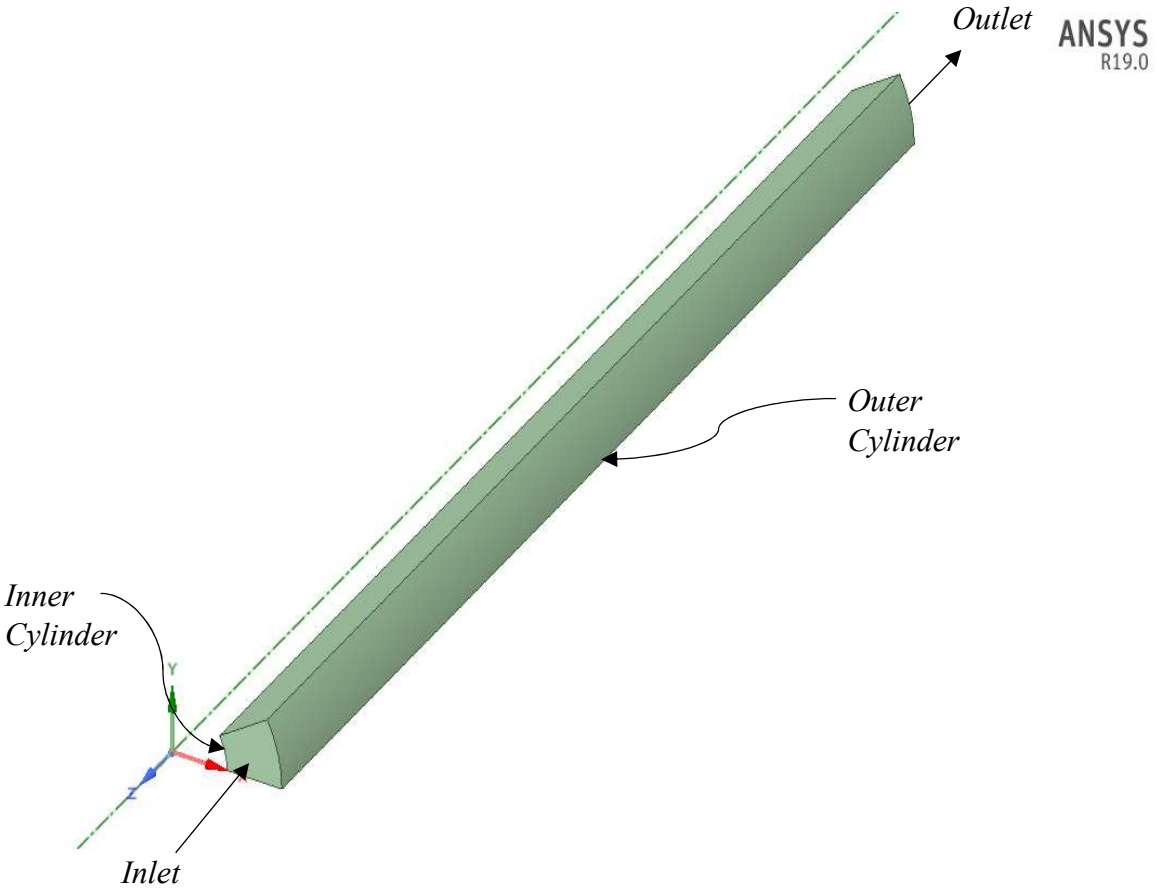

Figure 4-4 A 3D geometry for solving Couette flow

A structured mesh for the geometry in figure (4-4) is generated using the sweep method with the inlet and the outlet of the pipe as the source and the target respectively. Edge sizing with 20 divisions is applied to the arc formed by the inner cylinder. The length of the geometry is divided into 180 divisions. Figure (4-5) shows a zoomed-in image for the generated structured mesh used in Couette flow.

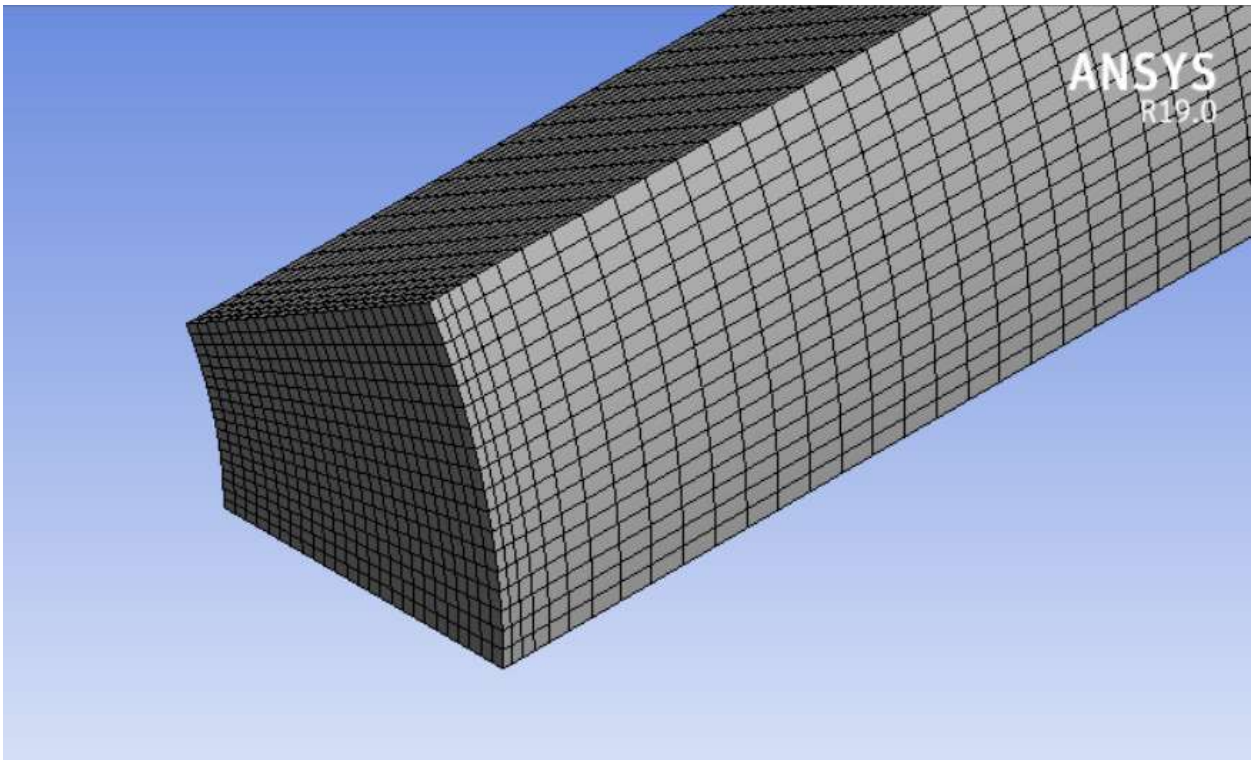

Figure 4-5 Mesh generated for the Couette flow simulation

The 3-dimensional geometry for the BSSD fluid domain consists of a concentric rotor-stator assembly of length 37.9 mm. The stator OD is fixed at 10.7 mm, whereas the rotor OD is varied on the size of the annular gap. An annular gap of 2.35 mm requires a rotor with 6 mm OD, whereas an annular gap of 1.35 mm an uses 8 mm OD rotor. The geometry is given a length of 20 mm (approximately twice of the OD of the stator) at the inlet and the outlet of the assembly for development of the flow. Figure (5-6) shows the geometry for the BSSD.

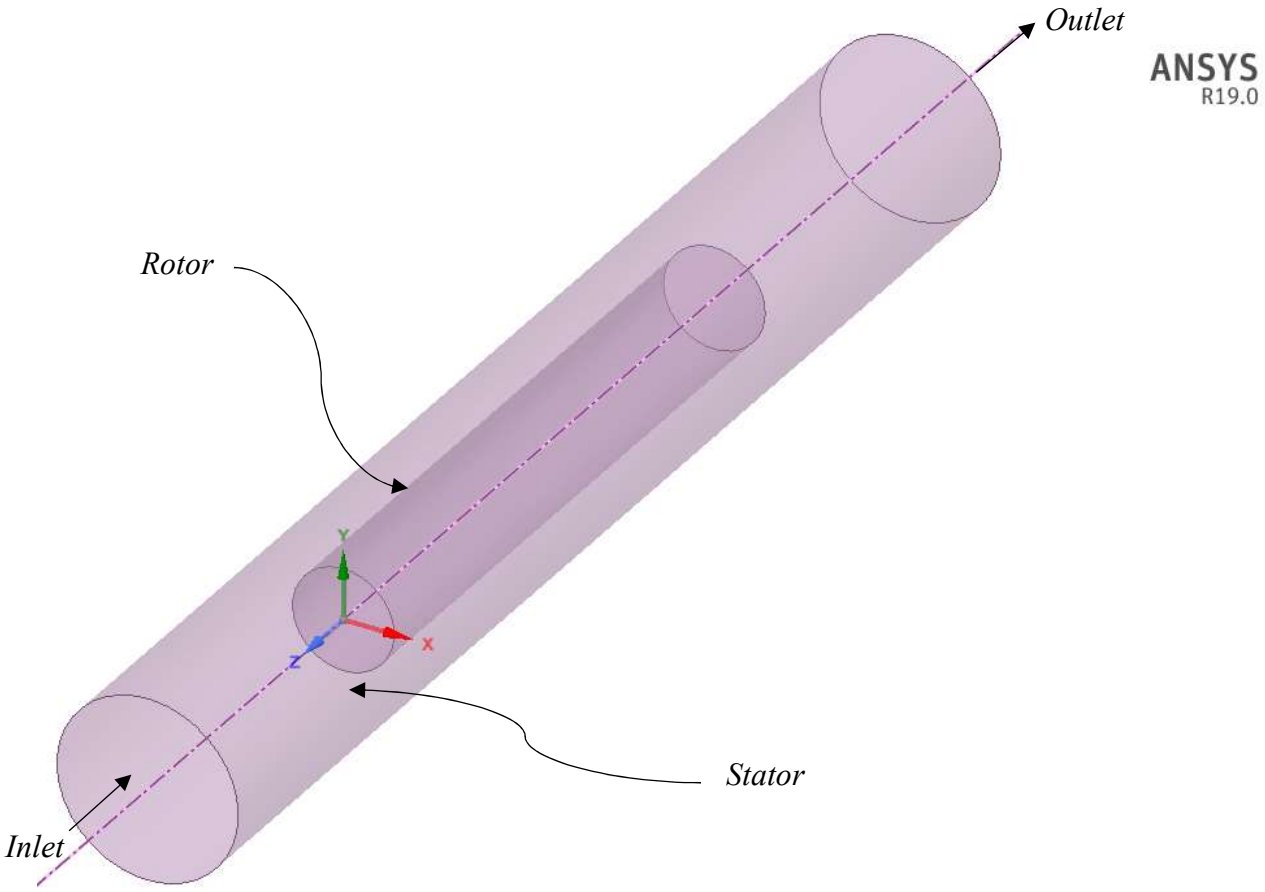

Figure 4-6 A 3D geometry for solving the flow through the BSSD

The patch conforming method is used to generate a tetrahedron mesh for the geometry shown in figure (4-6). The stator face is meshed using the face meshing feature with 250 internal divisions. Body sizing is applied to the fluid domain with element size 0.0005 m. Figure (4-7) shows the mesh generated in ANSYS Fluent R19.0.

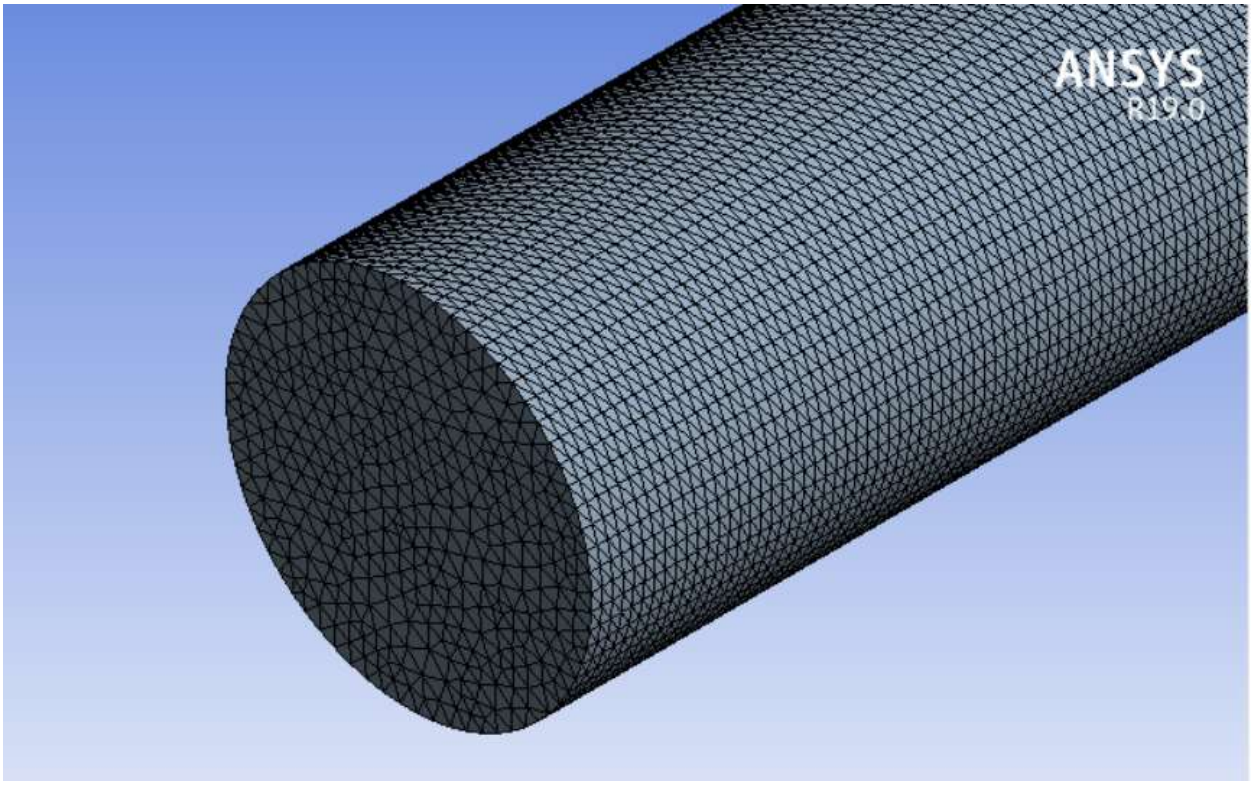

Figure 4-7 Mesh generated for solving the flow through BSSD

Section 1.2.2 elaborates the model setup for the (1) Poiseuille flow, (2) Couette flow, and (3) Flow through BSSD in ANSYS Fluent 19.0. The flow through the BSSD fluid domain is solved for 3 different flow rate values of the axial flow in 2 different annular gap sizes.

4.2.2 Model Setup

The steps taken towards the model setup for three different cases have been described as follows:

4.2.2.1 Poiseuille Flow

Steady state conditions are chosen for the simulation of Poiseuille flow through the circular cross section pipe described in section 1.2.1. The flow is considered to be laminar with Reynolds number calculated as follows

$$Re = \frac{\rho * V * D}{\mu}, \tag{4-8}$$

here ρ is the density of the fluid; 1 kg/m^3 , V is the axial velocity of the fluid, 1 m/s; D is the diameter of the pipe, 1 m and μ is the dynamic viscosity of the fluid, 0.002 kg/m-s.

The inlet is given a uniform velocity magnitude of 1 m/s as a boundary condition, whereas the outlet pressure is set to zero (0 Pa). A *SIMPLE* (acronym for the computational algorithm) solution method is selected with second order accuracy for pressure. The residual iteration monitors for continuity, and velocity in x, y, z directions are set to an absolute criteria of 1e-5 for convergence. The solution is initialized using a standard approach and convergence is achieved after about 320 iterations.

4.2.2.2 Couette flow

Steady state conditions are chosen for the simulation of the Couette flow through the geometry described in section 1.2.1. A laminar flow is assumed with circular Reynolds number calculated as

$$Re = \frac{\rho * \omega * R * h}{\mu}, \tag{4-9}$$

where ρ is the density of the fluid; 1 kg/m^3, ω is the angular velocity of the fluid, 0.8 rad/s; R is the radius of the inner rotating cylinder, 0.25 m; h is the annular gap available, 0.25 m and μ is the dynamic viscosity of the fluid, 0.002 kg/m-s.

The inlet and outlet for this geometry are assigned translational periodic condition, whereas a rotational periodic condition is assigned to the top and the base faces of the sector to be calculated as a complete circular cross-section. The inner cylinder wall is considered to be rotating at 0.8 rad/s angular velocity, and the outer cylinder wall is fixed and is given zero-velocity boundary condition. The Taylor number is set to be 1250 for comparison with equation (4-n). Again, the *SIMPLE* solution method is selected, with similar residual monitors for the continuity and velocity in x, y, z directions. In this case, convergence is achieved after about 1050 iterations.

4.2.2.3 Flow through BSSD

Transient conditions are chosen for the simulation of flow through the annular gap in the BSSD geometry described in section 1.2.1. Blood is modeled as an incompressible, non-Newtonian fluid with density of 1050 kg/m^3 and dynamic viscosity 0.0036 kg/m-s. The axial velocity and the axial Reynolds number are calculated using the following equations:

$$V = \frac{Q}{A}, \tag{4-10}$$

where V is the axial velocity, m/s; Q is the flow rate, m^3/s; A is the cross-sectional area, m^2 and

$$Re_{axial} = \frac{\rho * V * D}{\mu}, \tag{4-11}$$

where Re_{axial} is the axial Reynolds number, ρ is the density of blood, kg/m^3 , V is the axial velocity, m/s; D is the diameter, m and μ is the dynamic viscosity, kg/m-s. The values obtained are listed in the table below.

Table 4-2 List of values for Axial Reynolds number for the considered annular gap sizes

Flow rate, Q (mL/min)	OD of the rotor (mm)	Annular gap size (mm)	Axial Velocity (m/s)	Axial Reynolds number
100	6	2.35	0.033	103.531
100	8	1.35	0.059	184.055
200	6	2.35	0.066	207.062
200	8	1.35	0.118	368.110
300	6	2.35	0.100	310.592
300	8	1.35	0.177	552.164

The axial velocity and the axial Reynolds number are obtained using the same relations as above for the annular gap sizes. The circumferential Reynolds number calculated as per the equation (4-n) for the annular gap sizes is higher than the critical value for the laminar flow which suggests that flow is turbulent. Hence, k-omega SST model is chosen for solving medium to high rotational speeds.

The inlet is assigned a velocity-inlet boundary condition whereas the outlet pressure is zero (0 Pa). The moving rotor is given the rotational speed of 20000 rpm and the stator wall is given no-slip boundary condition. A *SIMPLE* solution method is selected with second order upwind transient formulation for accuracy. The residual monitors for the continuity, velocity in x, y, z directions, k and omega are set to an absolute criteria of 1e-6 for convergence. The solution is initialized using standard initialization from all zones and

is calculated with 1.67e-5 s as the time step size for 900-time steps. Each time step is iterated 20 times. Convergence is achieved after about 11000 iterations.

The highest shear stress is produced at the rotor wall of the BSSD. Hence, the wall shear stress is calculated when the blood comes in contact with the rotor wall is obtained. In order to calculate the index of hemolysis, the average wall shear stress is used in equation (4-2) and the blood damage is estimated with parameter variation. The exposure time is obtained by using

$$t = \frac{L*A}{Q}\ s, \tag{4-12}$$

where L is the length of the annulus, m.

4.3 Results

The results obtained after CFD modeling for the different geometries and flows are discussed in this section. The results for the Poiseuille flow and Couette flow are validated against the analytical solutions.

4.3.1 Poiseuille Flow

The figure (4-8) shows the change in velocity with respect to the length of the pipe. The mean velocity obtained numerically is 1.77 m/s is in agreement with the solution of the analytical equation. Figure (4-9) shows the velocity streamlines and the vectors at the outlet.

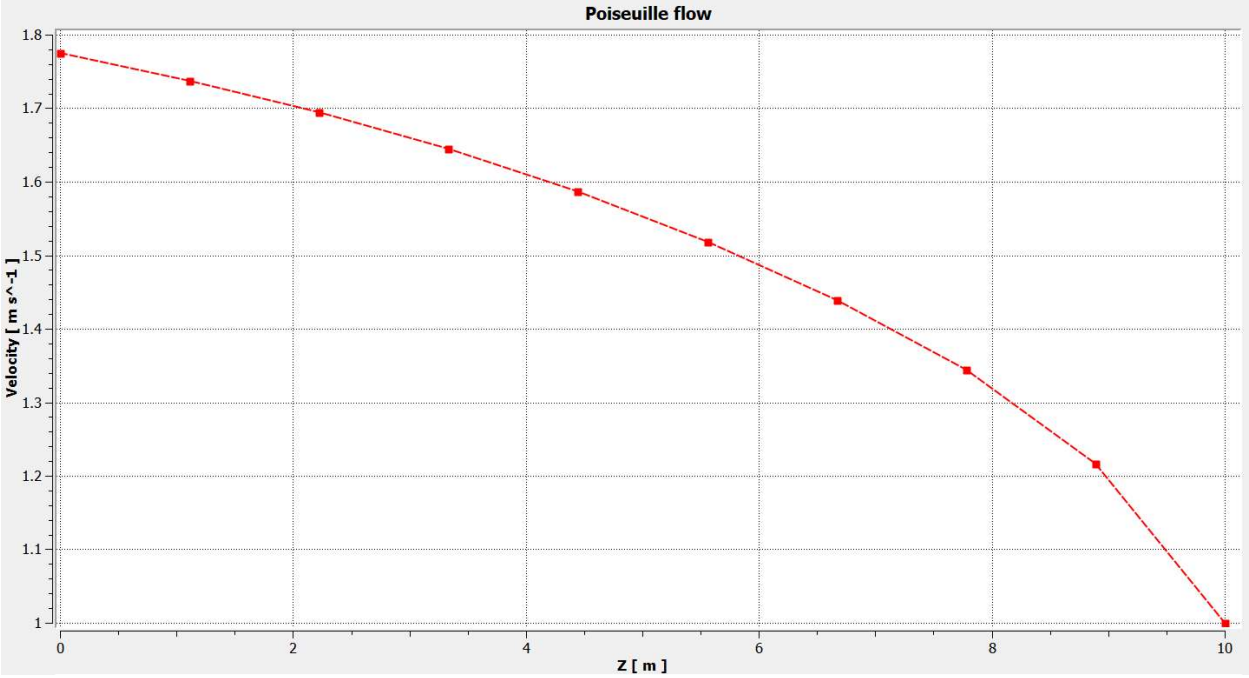

Figure 4-8 2D plot for change in velocity with length for Poiseuille flow

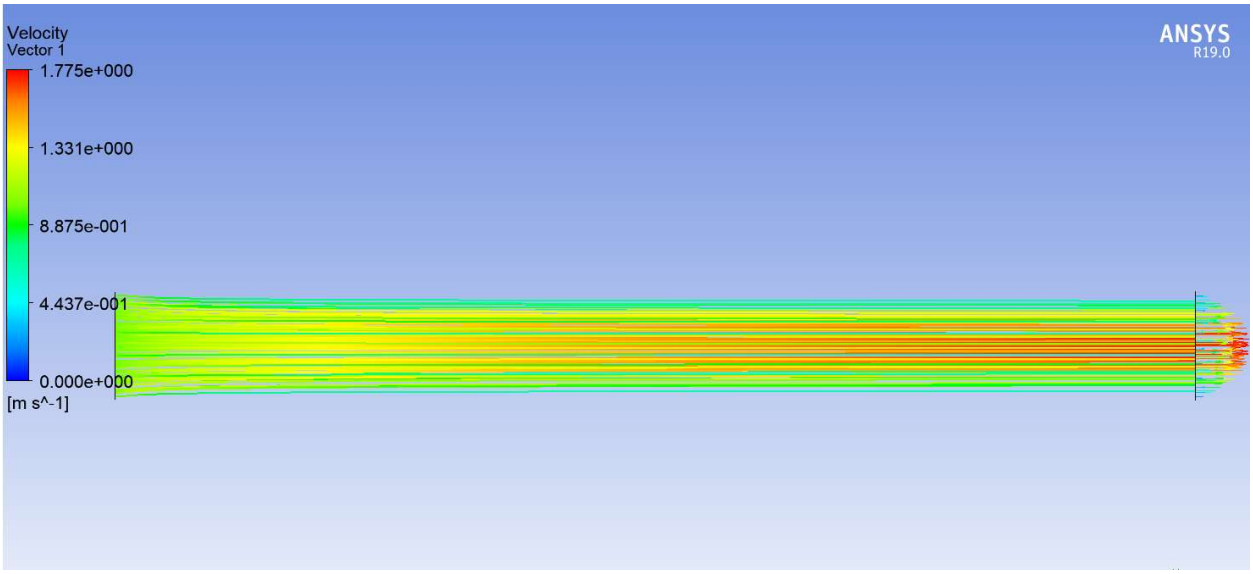

Figure 4-9 Velocity streamlines for the Poiseuille flow

4.3.2 Couette Flow

The calculated Taylor number is 1250, which is below the critical Taylor number 1708 [66]. Thus, Couette flow is observed in the figure (4-10).

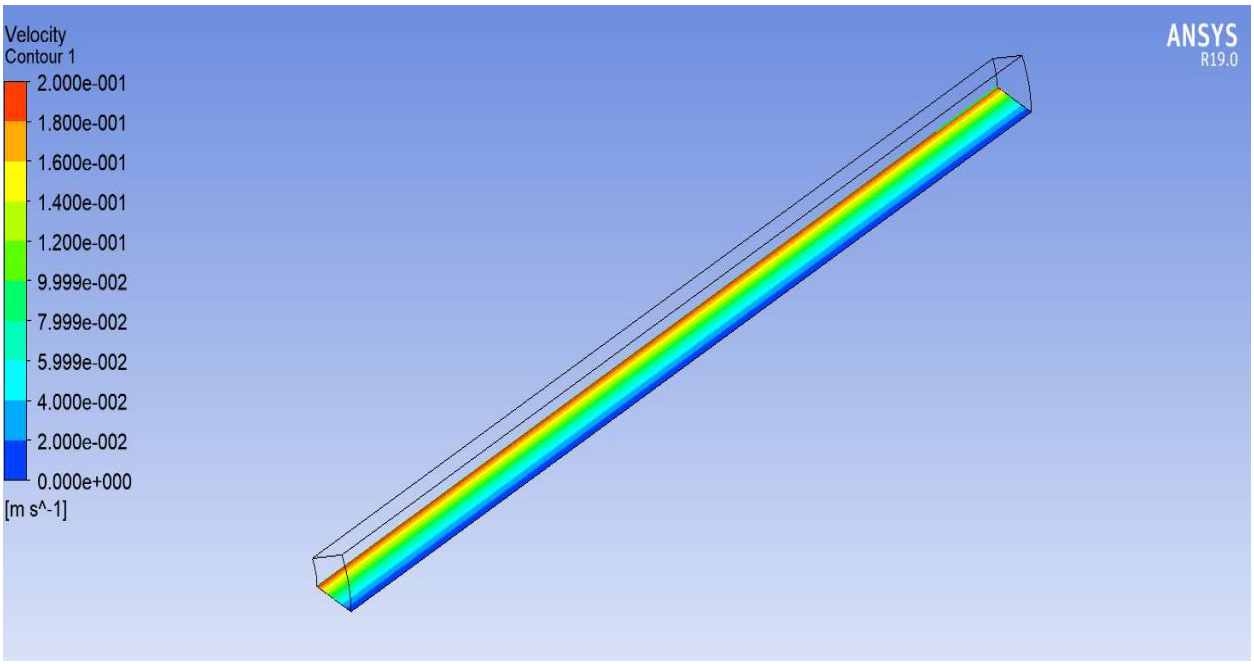

Figure 4-10 Velocity contour for Couette flow

4.3.3 Flow through BSSD

The wall shear stress is obtained from the CFD simulations for different flow rates and annular gap sizes for the BSSD flow domain. Table (4-2) lists the values for the average wall shear stress, exposure time and the index of hemolysis obtained after using equations (4-12) and (4-2).

Table 4-3 Outputs for flow through BSSD

Flow rate, Q (mL/min)	Rotor OD (mm)	Exposure time, t (s)	Mean Wall Shear Stress (Pa)	Index of Hemolysis (%)
100	8	0.901	221.27	0.54
100	6	1.401	197.36	0.57
200	8	0.451	222.52	0.34
200	6	0.701	172.74	0.28
300	8	0.300	223.81	0.27
300	6	0.467	171.99	0.21

Figure (4-11) shows the 3D surface plot for the analytical results obtained by the Zhang et. Al. [70] in 2011 and the CFD results obtained after simulating the flow through the BSSD.

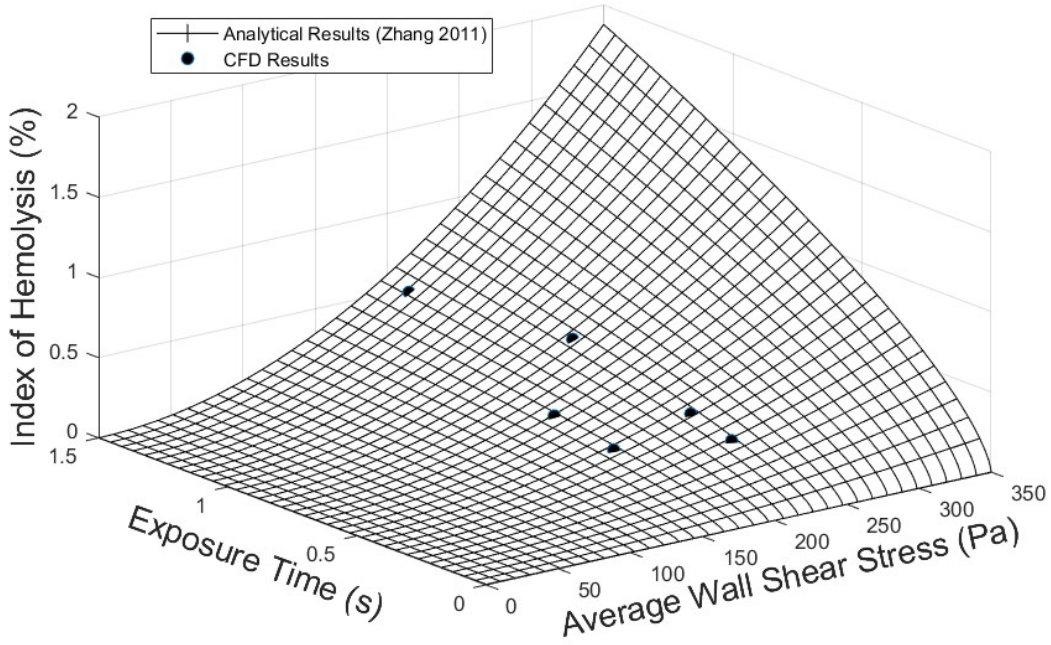

Figure 4-11 Hemolysis data from analytical equation and CFD simulations

The figure (4-12) displays the velocity contour for the 100 mL/min flow rate and 6 mm rotor OD.

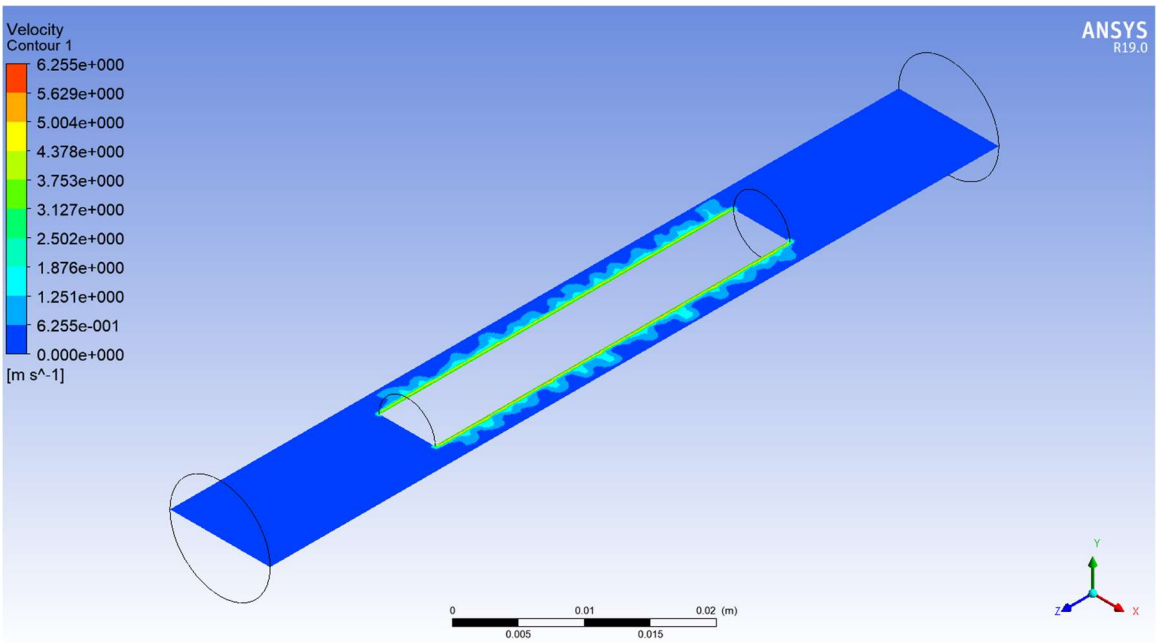

Figure 4-12 Velocity contour for the flow through the BSSD

4.4 Discussion

The Poiseuille flow results an error of about 3% between the analytical and numerical values for the mean velocity. The Couette flow is obtained at the Taylor number of 1250 which is lower than the critical value of 1708. This depicts the reliability of the CFD model. It can be interpreted from results for flow through the BSSD that the highest shear stress is obtained at the wall of the rotor. The average wall shear stress obtained from the CFD simulations suggests that it is the highest amount of shear stress that the blood will be exposed to in the BSSD during operation. Thus, the index of hemolysis obtained from the CFD calculations is the highest amount of hemolysis that this device can produce. As the flow rate increases, the exposure time for the blood decreases with which the index of hemolysis also decreases. Reduction in the annular gap results in the increase of the index of hemolysis for a given flow. The blood is subjected to higher amount of shear stress with the decrease in the annular gap size.

4.5 Conclusion

This study evaluates the CFD model to understand the effect of change in annular gap size and flow rates to estimate the blood damage in an operational BSSD. In order to achieve a reliable CFD model, separate cases for Poiseuille flow and Couette flow have been solved. For the flow through the BSSD, the average wall shear stress is obtained from the simulations which leads to calculating the index of hemolysis. This gives us an estimate of the caused blood damage. This data will be further used to modify the existing CFD model, as well as in choosing appropriate geometries and flow rates for the BSSD hemolysis testing for individual components of LVADs.

Chapter 5 Conclusion & Future Scope

5.1 Summary

In this thesis, "*Development of a Blood Shear Stress Device using Numerical and Experimental methods*", the motivation for pursuing this research has been stated in Chapter 1. The sub-systems and the functions of the BSSD are described in Chapter 2. Section 3.1 of Chapter 3 evaluates 27 geometries of concentric PM of varying OD of the inner PM ring, OD of the outer PM ring and their lengths for calculating the stiffness with respect to the displacement using numerical as well as experimental methods. The numerical results agree with the experimental results obtained by using magnetic force test rig. Section 3.2 of Chapter 3 studies 10 different BLDC motor sizes to estimate the radial stiffness with respect to the radial displacement as well as the evaluate the effect of change in rotor size on the back EMF and the torque constant. In Chapter 4, the CFD simulations for the blood flow through the BSSD are evaluated with varying flow rates and the annular gap sizes. The wall shear stress is calculated to estimate the highest index of hemolysis in the device. This research work lays the basis for the manufacturing of a blood shear stress device for individual component testing of LVADs for blood damage.

5.2 Future Scope

5.2.1 Detailed numerical model for Magnetic forces & Fluid flow

The existing magnetic numerical model for the PM rings and the BLDC motor evaluates the magnetic forces with respect to change in three degrees of freedom. The inclination of the PM rings in x and y direction has not been evaluated. A numerical magnetic model with PM rings attached to the BLDC motor would help in estimating the effect of the inclination of the PM rings on the magnetic forces generated as well as the

effect of other instabilities in the axial and the radial direction. Since, the passive maglev system and the BLDC motor two individual magnetic systems, the magnetic flux lines from each of them would interact with each other if the PM rings are attached directly to the BLDC motor and might disturb the magnetic levitation technology. Thus, we suggest using a non-magnetic spacer between the PM rings and the BLDC motor. The detailed numerical model can be used to estimate the size of this spacer by evaluating the magnetic forces.

The existing CFD models record the wall shear stress for evaluating the index of hemolysis. It would be useful to calculate the scalar shear stress on each particle of the blood by including particle tracking in the CFD model to get precise results for the index of hemolysis.

The BLDC motor – PM rings assembly is expected to have instabilities and lacks any form of damping. Thus, it would be valuable to integrate both the detailed models for the magnetic forces and the fluid flow as the blood will act as a viscous damping for the assembly. It would be useful to evaluate the effect of viscous damping on the instabilities and the magnetic forces produced due to them.

5.2.2 Particle Image Velocimetry (PIV) for flow through BSSD

Particle Image Velocimetry is an optical method of flow visualization to get instantaneous fluid properties like velocity, and stresses of fluids or individual particles. The data from the PIV could be used to validate the results from the detailed CFD model for the flow through the BSSD. This would aid in modelling a more robust CFD model for the BSSD.

5.2.3 Magnetic Force Test Rig Improvement

We experienced some unexpected issues while performing experimental analysis for the BLDC motor on the magnetic force test rig. The unexpected rise in the axial forces while the BLDC rotor is displaced radially is suspected to be due to the contact of the end of the motor rotor to the stator. In order to eliminate this issue, the magnetic force test rig can be improved by providing an arrangement to hold the rotor shaft from both its ends in an effective manner. The BLDC rotor shaft is held from a single end by the collet holder in the current test rig. Also, it would be useful to provide an arrangement on the top plate of the test rig to improve the visualization while aligning the BLDC motor.

5.2.4 Hemolysis testing

The hemolysis testing of the BSSD involves the connecting the BSSD in a blood shearing test loop designed by Dr. Chan. The blood would be driven by the CentriMag pump, and the hemolysis will be recorded. The hemolysis data is well documented for the CentriMag [80-86] which would allow separating the blood damage caused by BSSD. This would help in further improving the design of the BSSD.

5.2.5 Manufacturing and Assembly of BSSD

The final goal of this research would be to manufacture and assemble the BSSD after evaluating the inherent blood damage. This device will enable hemolysis testing for the individual components of any LVAD.

References

1. Pediatric Heart Specialists, "Normal Heart Anatomy and Blood Flow." https://pediatricheartspecialists.com/heart-education/14-normal/152-normal-heart-anatomy-and-blood-flow.

2. Editorial staff, "Difference between pulmonary and systemic circulation," https://difference.guru/difference-between-pulmonary-and-systemic-circulation/.

3. Mayo Clinic (2018), "Heart Valve Disease," https://www.mayoclinic.org/diseases-conditions/heart-valve-disease/symptoms-causes/syc-20353727.

4. InformedHealth.org, Cologne, Germany: Institute for Quality and Efficiency in Health Care (IQWiG), 2006, "Types of heart failure," https://www.ncbi.nlm.nih.gov/books/NBK481485.

5. Rekha Mankad, M.D., Mayo Clinic (2019),"Ejection fraction: What does it measure?," https://www.mayoclinic.org/ejection-fraction/expert-answers/faq-20058286.

6. American Heart Association, "Ejection fraction heart failure measurement," https://www.heart.org/en/health-topics/heart-failure/diagnosing-heart-failure/ejection-fraction-heart-failure-measurement.

7. Mayo Clinic, "Dilated Cardiomyopathy," https://www.mayoclinic.org/diseases-conditions/dilated-cardiomyopathy/symptomscauses/syc-20353149.

8. Mayo Clinic, "Hypertrophic cardiomyopathy," December 20, 2019 https://www.mayoclinic.org/diseasesconditions/hypertrophiccardiomyopathy/symptoms-causes/syc-20350198.

9. American Heart Association, "Classes of Heart Failure," https://www.heart.org/en/health-topics/heart-failure/what-is-heart-failure/classes-of-heart-failure.

10. Centers for Disease Control and Prevention, "Heart Failure," https://www.cdc.gov/heartdisease/heart_failure.htm.

11. Benjamin EJ, Muntner P, Alonso A, Bittencourt MS, Callaway CW, Carson AP, "Heart disease and stroke statistics—2019 update: a report from the American Heart Association," *Circulation*. 2019;139(10):e56–528.

12. Centers for Disease Control and Prevention National Center for Health Statistics, "Underlying Cause of Death, 1999–2017."

13. Cleveland Clinic, "Heart Failure: Understanding Heart Failure," https://my.clevelandclinic.org/health/diseases/17069-heart-failure-understanding-heart-failure.

14. Cleveland Clinic, "Heart Failure: Understanding Heart Failure: Management and Treatment," https://my.clevelandclinic.org/health/diseases/17069-heart-failure-understanding-heart-failure/management-and-treatment.

15. American Heart Association, "Lifestyle Changes for Heart Failure," https://www.heart.org/en/health-topics/heart-failure/treatment-options-for-heart-failure/lifestyle-changes-for-heart-failure.

16. United Network of Organ Sharing, "Transplants by organ type," 2020, https://unos.org/data/transplant-trends/transplants-by-organ-type/.

17. SynCardia, "What Are the Differences Between an LVAD and the TAH?," https://syncardia.com/patients/media/blog/2018/05/what-are-the-differences-between-an-lvad-and-the-tah/.

18. Kozik, D. J., & Plunkett, M. D. (2011), "Mechanical circulatory support," *Organogenesis*, 7(1), 50–63. https://doi:10.4161/org.7.1.14030.

19. Hosseinipour M, Gupta R, Bonnell M, Elahinia M, "Rotary mechanical circulatory support systems," *J Rehabil Assist Technol Eng*. 2017;4:2055668317725994. 2017 Sep 1. https://doi:10.1177/2055668317725994.

20. Gilotra NA, Stevens GR, "Temporary mechanical circulatory support: a review of the options, indications, and outcomes," *Clin Med Insights Cardiol*. 2015;8(Suppl 1):75–85. Published 2015 Feb 3. https://doi:10.4137/CMC.S15718.

21. Prinzing A, Herold U, Berkefeld A, Krane M, Lange R, Voss B, "Left ventricular assist devices-current state and perspectives," *J Thorac Dis.* 2016;8(8):E660–E666. https://doi:10.21037/jtd.2016.07.13.

22. Cooley DA, "The total artificial heart as a bridge to cardiac transplantation: personal recollections," *Texas Heart Inst J.* 2001;28(3):200–202.

23. Ahmed Alnajar and O.H. Frazier (2019), "The State of Artificial Heart Therapy," *Texas Heart Institute Journal*, February 2019, Vol. 46, No. 1, pp. 77-79. https://doi.org/10.14503/THIJ-18-6756.

24. DeBakey ME, "Left ventricular bypass pump for cardiac assistance: clinical experience," *Am J Cardiol.* 1971;27:3–11.

25. O. H. Frazier, MD, Timothy J. Myers, BS, Igor D. Gregoric, MD, Tehreen Khan, MD, Reynolds Delgado, MD, Mihai Croitoru, MD, Kathy Miller, BS , Robert Jarvik, MD,

Stephen Westaby, PhD, "Initial Clinical Experience With the Jarvik 2000 Implantable Axial-Flow Left Ventricular Assist System," *Circulation*. 2002;105:2855-2860 https://doi.org/10.1161/01.CIR.0000018167.47314.AF.

26. Frazier, O. H. (2014), "Mechanical circulatory assist device development at the Texas Heart Institute: A personal perspective," *Journal of Thoracic and Cardiovascular Surgery*, 147(6), 1738–1744. https://doi.org/10.1016/j.jtcvs.2014.04.019.

27. Han, J., & Trumble, D. R. (2019), "Cardiac assist devices: Early concepts, current technologies, and future innovations," *Bioengineering*, 6(1). https://doi.org/10.3390/bioengineering6010018.

28. Kozik, D. J., & Plunkett, M. D. (2011), "Mechanical circulatory support," *Organogenesis*, 7(1), 50–63. https://doi.org/10.4161/org.7.1.14030.

29. Kirklin, J. K., & Naftel, D. C. (2008), "Mechanical circulatory support: registering a therapy in evolution," *Circulation*. Heart Failure, 1(3), 200–205. https://doi.org/10.1161/CIRCHEARTFAILURE.108.782599.

30. Lindseth, R. O. (2002), "The Next Wave of Mechanical Circulatory Support Devices," *Cardiac Interventions Today*, 9(12), 9–15. https://doi.org/10.1190/1.1439710

31. Wang, Y., Logan, T. G., Smith, P. A., Hsu, P. L., Cohn, W. E., Xu, L., & McMahon, R. A. (2017), " Systematic Design of a Magnetically Levitated Brushless DC Motor for a Reversible Rotary Intra-Aortic Blood Pump," *Artificial Organs*, 41(10), 923–933. https://doi.org/10.1111/aor.12965

32. Ravaud, R., Lemarquand, G., & Lemarquand, V. (2009), "Force and stiffness of passive magnetic bearings using permanent magnets. part 2: Radial magnetization," *IEEE*

Transactions on Magnetics, 45(9), 3334–3342. https://doi.org/10.1109/TMAG.2009.2025315.

33. Kurita, N., Ishikawa, T., Saito, N., Masuzawa, T., & Timms, D. L. (2019), "A Double-Sided Stator Type Axial Bearingless Motor Development for Total Artificial Heart," *IEEE Transactions on Industry Applications*, 55(2), 1516–1523. https://doi.org/10.1109/TIA.2018.2884609.

34. Kurita, N., Ishikawa, T., Takada, H., & Suzuki, G. (2015), "Proposal of a permanent magnet hybrid-type axial magnetically levitated motor," *IEEE Journal of Industry Applications*, 4(4), 339–345. https://doi.org/10.1541/ieejjia.4.339.

35. Mitterhofer, H., Gruber, W., & Amrhein, W. (2014), "On the high-speed capacity of bearingless drives," *IEEE Transactions on Industrial Electronics*, 61(6), 3119–3126. https://doi.org/10.1109/TIE.2013.2272281.

36. Gruber, W., Grabner, H., Silber, S., & Amrhein, W. (2014), "Design of a brushless permanent-magnet synchronous drive with a purely passively suspended rotor," *IEEE Transactions on Industry Applications*, 50(5), 3258–3264. https://doi.org/10.1109/TIA.2014.2308351.

37. Bauer, W., & Amrhein, W. (2014), "Electrical design considerations for a bearingless axial-force/torque motor," *IEEE Transactions on Industry Applications*, 50(4), 2512–2522. https://doi.org/10.1109/TIA.2014.2300415.

38. Asama, J., Kanehara, D., Oiwa, T., & Chiba, A. (2014), "Development of a compact centrifugal pump with a two-axis actively positioned consequent-pole bearingless motor," *IEEE Transactions on Industry Applications*, 50(1), 288–295. https://doi.org/10.1109/TIA.2013.2270452.

39. Tezuka, T., Kurita, N., & Ishikawa, T. (2013). "Design and simulation of a five degrees of freedom active control magnetic levitated motor," *IEEE Transactions on Magnetics*, 49(5), 2257–2262. https://doi.org/10.1109/TMAG.2013.2242452.

40. Reichert, T., Kolar, J. W., & Nussbaumer, T. (2013). "Stator tooth design study for bearingless exterior rotor PMSM," *IEEE Transactions on Industry Applications*, 49(4), 1515–1522. https://doi.org/10.1109/TIA.2013.2257975.

41. Asama, J., Hamasaki, Y., Oiwa, T., & Chiba, A. (2013). Proposal and analysis of a novel single-drive bearingless motor. *IEEE Transactions on Industrial Electronics*, 60(1), 129–138. https://doi.org/10.1109/TIE.2012.2183840.

42. Yang, S. M. (2011). "Electromagnetic actuator implementation and control for resonance vibration reduction in miniature magnetically levitated rotating machines," *IEEE Transactions on Industrial Electronics*, 58(2), 611–617. https://doi.org/10.1109/TIE.2010.2046000.

43. Nussbaumer, T., Karutz, P., Zurcher, F., & Kolar, J. W. (2011). "Magnetically levitated slice motors-An overview," *IEEE Transactions on Industry Applications*, 47(2), 754–766. https://doi.org/10.1109/TIA.2010.2102731.

44. Asama, J., Asami, T., Imakawa, T., Chiba, A., Nakajima, A., & Rahman, M. A. (2011). "Effects of permanent-magnet passive magnetic bearing on a two-axis actively regulated low-speed bearingless motor," *IEEE Transactions on Energy Conversion*, 26(1), 46–54. https://doi.org/10.1109/TEC.2010.2073709.

45. Karutz, P., Nussbaumer, T., Gruber, W., & Kolar, J. W. (2008). "Novel magnetically levitated two-level motor," *IEEE/ASME Transactions on Mechatronics*, 13(6), 658–668. https://doi.org/10.1109/TMECH.2008.2004344.

46. Ueno, S., & Okada, Y. (2000). "Characteristics and control of a bidirectional axial gap combined motor-bearing," *IEEE/ASME Transactions on Mechatronics*, 5(3), 310–318. https://doi.org/10.1109/3516.868923.

47. Wang, F., Wang, J., Kong, Z., & Zhang, F. (2004). "Radial and axial force calculation of BLDC motor with passive magnetic bearing," *Conference Proceedings - IPEMC 2004: 4th International Power Electronics and Motion Control Conference*, 1(59977014), 290–293.

48. COMSOL Multiphysics. (2017). *AC/DC Module User's Guide.*

49. James, M. E., Papavassiliou, D. V., & O'Rear, E. A. (2019). "Use of computational fluid dynamics to analyze blood flow, hemolysis and sublethal damage to red blood cells in a bileaflet artificial heart valve," *Fluids*, 4(1). https://doi.org/10.3390/fluids4010019.

50. Paul R, Apel J, Klaus S, Schügner F, Schwindke P, Reul H. "Shear stress related blood damage in laminar couette flow," *Artif Organs* 2003;27:517–29.

51. Fraser, K. H., Taskin, M. E., Griffith, B. P., & Wu, Z. J. (2011). "The use of computational fluid dynamics in the development of ventricular assist devices," *Medical Engineering and Physics*, 33(3), 263–280. https://doi.org/10.1016/j.medengphy.2010.10.014.

52. Fraser, K. H., Zhang, T., Taskin, M. E., Griffith, B. P., & Wu, Z. J. (2012). "A quantitative comparison of mechanical blood damage parameters in rotary ventricular assist devices: Shear stress, exposure time and hemolysis index," *Journal of Biomechanical Engineering*, 134(8), 1–11. https://doi.org/10.1115/1.4007092.

53. Zhang, J., Gellman, B., Koert, A., Dasse, K. A., Gilbert, R. J., Griffith, B. P., & Wu, Z. J. (2006). Computational and experimental evaluation of the fluid dynamics and hemocompatibility of the centrimag blood pump," *Artificial Organs*, 30(3), 168–177. https://doi.org/10.1111/j.1525-1594.2006.00203.

54. Gross-Hardt, S., Boehning, F., Steinseifer, U., Schmitz-Rode, T., & Kaufmann, T. A. S. (2019). "Mesh sensitivity analysis for quantitative shear stress assessment in blood pumps using computational fluid dynamics mesh sensitivity analysis for quantitative shear stress assessment in blood pumps using computational fluid dynamics," *Journal of Biomechanical Engineering*, 141(2), 1–8. https://doi.org/10.1115/1.4042043.

55. Lynch, E. C. (1972). "Red blood cell damage by shear stress," *Biophys J* 1972. 12, 257–273.

56. Wu, J., Antaki, J. F., Snyder, T. A., Wagner, W. R., Borovetz, H. S., & Paden, B. E. (2005). Design optimization of blood shearing instrument by computational fluid dynamics. *Artificial Organs*, 29(6), 482–489. https://doi.org/10.1111/j.1525-1594.2005.29082.

57. Giersiepen, M., Wurzinger, L.J., Opitz, R., & Reul, H. (1990). "Estimation of Shear Stress-related Blood Damage in Heart Valve Prostheses - in Vitro Comparison of 25 Aortic Valves," *The International Journal of Artificial Organs*, 13, 300 - 306.

58. Mitoh, A., Yano, T., Sekine, K., Mitamura, Y., Kim, D. W., Yozu, R., & Okamoto, E. (2002). "Computational fluid dynamics analysis of an intra-cardiac axial flow pump," *Proceedings of Asian Simulation Conference; System Simulation and Scientific Computing (Shanghai)*, 2(1), 1032–1034.

59. Paul, R., Apel, J., Klaus, S., Schügner, F., Schwindke, P., & Reul, H. (2003). "Shear stress related blood damage in laminar Couette flow," *Artificial Organs*, 27(6), 517–529. https://doi.org/10.1046/j.1525-1594.2003.07103.

60. Smith, R. E., Smith, P. A., & Cohn, W. E. (2017). "Predicting the Dimensions of an Intracardiac Partial-Assist Pump for Percutaneous Delivery by Analytical and Numerical Methods," *Cardiovascular Engineering and Technology*, 8(4), 453–464. https://doi.org/10.1007/s13239-017-0331-0.

61. Smith, P. A., Wang, Y., Bieritz, S. A., Sampaio, L. C., Cohn, W. E., Metcalfe, R. W., & Frazier, O. H. (2019). "Design Method Using Statistical Models for Miniature Left Ventricular Assist Device Hydraulics," *Annals of Biomedical Engineering*, 47(1), 126–137. https://doi.org/10.1007/s10439-018-02140-w.

62. Smith, P. A., Wang, Y., Bieritz, S. A., Sampaio, L. C., Metcalfe, R. W., Cohn, W. E., & Frazier, O. H. (2018). "Hemodynamic Evaluation of an Intra-Atrial Blood Pump on a Pulsatile Mock Circulatory Loop," *Proceedings of the Annual International Conference of the IEEE Engineering in Medicine and Biology Society, EMBS*, 2018-July, 4508–4511. https://doi.org/10.1109/EMBC.2018.8513133.

63. Smith, P. A., Wang, Y., Bieritz, S. A., Conger, J. L., Sampaio, L. C., Cohn, W. E., & Frazier, O. H. (2018). "In Vivo Feasibility Study of an Intra-Atrial Blood Pump for Partial Support of the Left Ventricle," *Proceedings of the Annual International Conference of the IEEE Engineering in Medicine and Biology Society, EMBS*, 2018-July, 4520–4523. https://doi.org/10.1109/EMBC.2018.8513193.

64. Alex Smith, P., Wang, Y., Metcalfe, R. W., Sampaio, L. C., Timms, D. L., Cohn, W. E., & Frazier, O. H. (2018). "Preliminary design of the internal geometry in a minimally

invasive left ventricular assist device under pulsatile-flow conditions," *International Journal of Artificial Organs*, 41(3), 144–151. https://doi.org/10.1177/0391398817752291.

65. Taskin, M. E., Fraser, K. H., Zhang, T., Wu, C., Griffith, B. P., & Wu, Z. J. (2012). "Evaluation of Eulerian and Lagrangian models for hemolysis estimation," *ASAIO Journal*, 58(4), 363–372. https://doi.org/10.1097/MAT.0b013e318254833b.

66. Taylor, G. I. (1923). "Two Rotating Cylinders," *Philosophical Transactions of Rhe Royal Society of London*. Series A, Containing Papers of a Mathematical or Physical Character, 223(1923), 289–343.

67. Taskin, M. E., Fraser, K. H., Zhang, T., Gellman, B., Fleischli, A., Dasse, K. A., Griffith, B. P., & Wu, Z. J. (2010). "Computational Characterization of Flow and Hemolytic Performance of the UltraMag Blood Pump for Circulatory Support," *Artificial Organs*, 34(12), 1099–1113. https://doi.org/10.1111/j.1525-1594.2010.01017.

68. Yano, T., Sekine, K., Mitoh, A., Mitamura, Y., Okamoto, E., Kim, D. W., Nishimura, I., Murabayashi, S., & Yozu, R. (2003). "An Estimation Method of Hemolysis within an Axial Flow Blood Pump by Computational Fluid Dynamics Analysis," *Artificial Organs*, 27(10), 920–925. https://doi.org/10.1046/j.1525-1594.2003.00034.

69. Yano, T., Sekine, K., Mitoh, A., Mitamura, Y., Okamoto, E., Kim, D. W., Nishimura, I., Murabayashi, S., & Yozu, R. (2003). "An Estimation Method of Hemolysis within an Axial Flow Blood Pump by Computational Fluid Dynamics Analysis," *Artificial Organs*, 27(10), 920–925. https://doi.org/10.1046/j.1525-1594.2003.00034.

70. Zhang, T., Taskin, M. E., Fang, H. Bin, Pampori, A., Jarvik, R., Griffith, B. P., & Wu, Z. J. (2012). "Study of flow-induced hemolysis using novel couette-type blood-shearing devices," *Artificial Organs*, 35(12), 1180–1186. https://doi.org/10.1111/j.1525-1594.2011.01243.

71. Arvand, A., Hormes, M., & Reul, H. (2005). "A validated computational fluid dynamics model to estimate hemolysis in a rotary blood pump," *Artificial Organs*, 29(7), 531–540. https://doi.org/10.1111/j.1525-1594.2005.29089.

72. Couette, M. (1890) Études sur le frottement des liquids, Ann. Chim. Phys. 6, Ser. 21, 433-510.

73. M. Monfared, E. Shirani, F. Aloui, M. R. Salimpour (2015), "Numerical and Experimental Study on the Effects of Taylor Number on the Wavelength of the Couette-Taylor Flow."

74. Mallock, A. (1888). "Determination of the viscosity of water," Proc. Royal Soc. London, 45,126-132.

75. Newton, I. (1934). "The Motion of Bodies, Principia: Vol. 1, F. Cajori, ed.," U. Calif. Press, Berkeley, 385386.

76. Rayleigh, L. (1916) on the dynamics of revolving fluids, Proc. Royal Soc. A, 93:148-154.

77. Stokes, G. (1880). "Mathematical and Physical Papers, 1," Cambridge Univ. Press, Cambridge, England, 102-104.

78. Taylor, G. I. (1923) "Stability of a viscous liquid contained between two rotating cylinders," Philos. Trans. R. Soc. London, Ser. A, 223:289-343.

79. Rotating Cylinders, Annuli, and Spheres, Rotating Flow, https://doi: 10.1016/B978-0-12-382098-3.00006-8.

80. Chan, C. H. H., Diab, S., Moody, K., Frazier, O. H., Sampaio, L. C., Fraser, C. D., Teruya, J., & Adachi, I. (2018). "In Vitro Hemocompatibility Evaluation of Ventricular Assist Devices in Pediatric Flow Conditions: A Benchmark Study," *Artificial Organs*, 42(11), 1028–1034. https://doi.org/10.1111/aor.13165.

81. Chan, C. H. H., Pieper, I. L., Robinson, C. R., Friedmann, Y., Kanamarlapudi, V., & Thornton, C. A. (2017). "Shear Stress-Induced Total Blood Trauma in Multiple Species," *Artificial Organs*, 41(10), 934–947. https://doi.org/10.1111/aor.12932.

82. Chan, C. H. H., Pieper, I. L., Hambly, R., Radley, G., Jones, A., Friedmann, Y., Hawkins, K. M., Westaby, S., Foster, G., & Thornton, C. A. (2015). "The CentriMag Centrifugal Blood Pump as a Benchmark for In Vitro Testing of Hemocompatibility in Implantable Ventricular Assist Devices," *Artificial Organs*, 39(2), 93–101. https://doi.org/10.1111/aor.12351.

83. Chan, C. H. H., Hilton, A., Foster, G., & Hawkins, K. (2012). "Reevaluation of the harboe assay as a standardized method of assessment for the hemolytic performance of ventricular assist devices," *Artificial Organs*, 36(8), 724–730. https://doi.org/10.1111/j.1525-1594.2012.01515.

84. Chan, C. H. H., Pieper, I. L., Hambly, R., Radley, G., Jones, A., Friedmann, Y., Hawkins, K. M., Westaby, S., Foster, G., & Thornton, C. A. (2015). "The CentriMag Centrifugal Blood Pump as a Benchmark for In Vitro Testing of Hemocompatibility in Implantable Ventricular Assist Devices," *Artificial Organs*, 39(2), 93–101. https://doi.org/10.1111/aor.12351.

85. Chan, C. H. H., Hilton, A., Foster, G., & Hawkins, K. (2012). "Reevaluation of the harboe assay as a standardized method of assessment for the hemolytic performance of ventricular assist devices," *Artificial Organs*, 36(8), 724–730. https://doi.org/10.1111/j.1525-1594.2012.01515.

86. Chan, C. H. H., Nandakumar, D., Balletti, N., Horobin, J., Wu, E. L.-J., Bouquet, M., Stephens, A., Pauls, J. P., Tansley, G., Fraser, J. F., Simmonds, M. J., & Gregory, S. D. (2019). "In Vitro Hemocompatibility Evaluation of Modified Rotary Left to Right Ventricular Assist Devices in Pulmonary Flow Conditions," *ASAIO Journal, 1*. https://doi.org/10.1097/mat.0000000000001049.